

## Research Article

# Template Synthesis of Ni(II) and Zn(II) Complexes Derived from $N_2O_2$ Donor Symmetrical Tetradentate Ligands System: Comparative Antioxidant, Xanthine inhibitory, and Computational Studies

Ibrahim Waziri<sup>1\*</sup>, Grema A. Mala<sup>1</sup>, Ibrahim M. Wakil<sup>1</sup>, Louis-Charl C. Coetzee<sup>2</sup>, Hussein Garba<sup>1</sup>

<sup>1</sup>Department of Pure and Applied Chemistry, University of Maiduguri, P.M.B. 1069, Maiduguri, Nigeria

<sup>2</sup>Department of Chemical Sciences, University of Johannesburg, P.O. Box 524, Auckland Park 2006, South Africa.

\*Corresponding author: [triumph2236@gmail.com](mailto:triumph2236@gmail.com), [doi.org/10.55639/607.2737](https://doi.org/10.55639/607.2737)

### ARTICLE INFO:

#### Keywords:

Metal complexes,  
Schiff bases,  
*In-situ* synthesis,  
Free radicals,  
Xanthine oxidase

### ABSTRACT

Four mononuclear symmetric coordination compounds of Ni(II) and Zn(II) (C1–C4), obtained from  $N_2O_2$  donor Schiff base ligand systems were synthesized *in-situ* and characterized with a variety of analytical and spectroscopic techniques such as elemental CHN-analysis, <sup>1</sup>H-NMR, <sup>13</sup>C{H}NMR, UV-Visible, Infrared, powder X-ray diffraction, scanning electron, and high-resolution mass spectroscopies. These analyses revealed that the ligands chelate the metal ions through the oxygen and nitrogen ( $N_2O_2$ ) atoms of the phenolate and azomethine functional groups, resulting in distorted and perfect square planar geometry around Zn(II) and Ni(II) ions, respectively. The 2,2-diphenylpicrylhydrazyl (DPPH) radical scavenging and xanthine oxidase activity of the complexes were investigated using *in vitro* assay techniques. The studies revealed that the complexes possess moderate radical scavenging activity with no or very weak xanthine oxidase activity, in which the controls show better activity than the complexes in both assays. However, C3 and C1 demonstrated some level of activity at higher concentrations but not commensurate with the controls. The DFT calculation of the complexes using the M06-2X/B3LYP-311G9d.p) level of the theory presented electronic properties that supported the experimental findings on the complexes.

Corresponding author: Ibrahim Waziri Email: [triumph2236@gmail.com](mailto:triumph2236@gmail.com)

Department of Pure and Applied Chemistry, University of Maiduguri, Borno State, Nigeria

## INTRODUCTION

Coordination compounds obtained from tetra dentate Schiff base ligands are becoming increasingly popular. They've been widely used as catalysts of choice for a variety of organic reactions, electrochemical reaction processes (Soroceanu and Bargan, 2022), specialized synthesis (Yusuf *et al.*, 2021), biological activity (Nguyen *et al.*, 2021; Saranya *et al.*, 2020), and as chemical sensors (Salih *et al.*, 2021). Because of their remarkable therapeutic properties, nickel and zinc complexes derived from tetra dentate Schiff bases have gained attention (Abdel-Rahman *et al.*, 2022; Kargar *et al.*, 2021). Consequently, comparative biological studies of these compounds have received little attention. These complexes have been shown to have luminescent properties, particularly those formed by salen ligands. The core properties of coordination compounds are determined by types of the ligands and metal centres (Haas and Franz, 2009; Jay *et al.*, 2018). The metal complex design provides an efficient method for developing potential new therapeutic agents (Ashiq *et al.*, 2021; Karges and Cohen, 2021). Furthermore, because most of the complexes reported are synthesized *ex-situ* (preparing ligand before reacting with the metal ion via a two-step process), low yield is a major factor affecting this synthetic method, and only a few of the reported complexes are synthesized *in-situ* (one pot synthesis) (Guo *et al.*, 2014; Luo *et al.*, 2022; Terraschke *et al.*, 2018). In addition, the two pot synthesis (*ex-situ*) method is more desirable for large scale synthesis (Demaerel *et al.*, 2020). However, in the laboratory, reactions are typically performed at a lower scale before optimization, which presents challenges due to the low yield of the *ex-situ* method. Hence, the *in-situ* method is preferable at this stage of the reaction.

*In-situ* synthesis is a simple and efficient method of synthesis. This strategy allows for concurrent complex formation using *in-situ* formed complexes from the corresponding

starting materials (Adnan *et al.*, 2018; Liu *et al.*, 2015). The ligand and complex will be formed in this case in a one-pot reaction system. This route has the advantage of producing a high yield while saving time (Kong *et al.*, 2019; Lind *et al.*, 2022). Yet, one disadvantage of this strategy is that the byproduct educts of the *in-situ* reaction may occasionally alter the composition of the final product (Elsebach *et al.*, 2020). This occurs only in rare cases and can be avoided by determining the actual limiting reagent among the precursors prior to the start of the reaction. It is on this note that this study reported the *in-situ* synthesis of symmetrical Ni(II) and Zn(II) complexes from tetra dentate ( $N_2O_2$ ) donor Schiff bases using salicylaldehyde, ortho-phenylenediamine, and ethylenediamine, as well as the corresponding metal salts of Ni(II) and Zn(II). A DPPH radical scavenging and Xanthine inhibitory assays were used to compare the antioxidant and Xanthine inhibitory properties of the synthesized complexes as viable candidates for neurodegenerative diseases.

The presence of radicals in the biological system plays a significant role in the development of diseases affecting the functions and structures of the body's organs (Dubois-Deruy *et al.*, 2020; Oliverio *et al.*, 2022; Sharifi-Rad *et al.*, 2020). In contrast, xanthine oxidase plays an important role in the development of diseases that affect the lungs or cause difficulty in breathing. (Almagro *et al.*, 2020; Feoli *et al.*, 2014). It also facilitates the generation of reactive nitrogen species that interact with DNA, causing cellular damage (Battelli *et al.*, 2016). To date, several Xanthine inhibitors and radical scavengers have been reported, the majority of which are organic in nature. Unfortunately, these compounds are linked to a variety of side effects, including nausea, diarrhea, headaches, and so on (Minh *et al.*, 2019).

Copper complexes derived from Schiff base ligand were found to be potent Xanthine

inhibitors with an  $IC_{50}$  of (0.43-2.25 M) (Li *et al.*, 2007). Similarly, some molybdenum complexes have been shown to inhibit Xanthine (Chaves *et al.*, 2008; Kirk and Hille, 2022). As a result, metal-based compounds that act as both free radical scavengers and Xanthine inhibitors are required to have a dual effect on the oxidation process within the body system.

## EXPERIMENTAL

### Materials and reagents

All the reagents utilized in the study were obtained from Merck Life Science (Pty) Ltd. They are of analytical grade and were used without further purification.

### Physical measurements

Melting points were recorded using MEL-TEMP electro-thermal apparatus (model: 1002D) without being corrected. Infra-red spectra were recorded using a Tensor 27 Bruker and Perkin-Elmer FT-IR spectrometer Bx. Elemental content (CHN) was measured using a VarioElementar III microbe CHNS analyser. Electronic spectra were obtained on a UV-1900 Shimadzu UV-Visible spectrometer at room temperature. NMR experiments (1D and 2D) were performed on a Bruker-500 MHz spectrometer (500 MHz for  $^1H$  and 125 MHz for  $^{13}C$ ). DMSO- $d_6$  was used for both the proton and carbon analyses. The chemical shifts are expressed as part per million (ppm) referenced to DMSO- $d_6$ , at  $\delta_H =$

2.50 and  $\delta_C = 39.50$ , for  $^1H$  NMR and  $^{13}C\{H\}$  NMR spectra, respectively. Powder X-ray diffraction analysis data were collected using a Rigaku miniFlex600 benchtop model with Cu- $K\alpha$  radiation ( $\lambda = 1.5418 \text{ \AA}$ ) over  $2\theta$  range of  $0-80^\circ$  at room temperature. Mass spectra were obtained using high resolution mass spectrometry on a WatersAcquity UPLC Synapt G2HD machine. The thermogravimetric analysis was conducted on a STDQ600 thermoanalyzer with a heating rate of  $10^\circ C \cdot min^{-1}$  under nitrogen flow.

### Synthesis of the complexes

#### General procedures

An *in-situ* method was used to synthesize the complexes (Dehkhodaei *et al.*, 2017). In a separate reaction flask, a methanolic solution (15 mL) of salicylaldehyde (0.4886 g, 4 mmol, 2 eq) was added dropwise to methanolic solutions (15 mL) of ethylenediamine (0.1202 g, 2 mmol, 1 eq) and ortho phenylenediamine (0.2163 g, 2 mmol, 1 eq). Methanolic solutions (15 mL) of either zinc nitrate hexahydrate (0.5950 g, 2 mmol, 1 eq) or nickel chloride hexahydrate (0.5810 g, 2 mmol, 1 eq) were added to each of the above mixtures and stirred for 6 h under inert conditions ( $N_2$ ) at ambient temperature. The resulting precipitate obtained was separated, washed using the reaction solvent and hexane, and dried under  $P_2O_5$ .

#### 2,2'-((1E, 1E)-(1,2-phenylenebis(azanylylidene))bis(methanylylidene))diphenolatenickel(II) (C1)

Dark brown solid; Yield: (0.3951 g, 87 %), mp:  $240^\circ C$ ;  $^1H$  NMR (500 MHz, DMSO- $d_6$ ):  $\delta_H$  (ppm): 6.68 (t, 2H,  $J_{HH} = 7.0$  Hz, Ar), 6.88 (d, 2H,  $J_{HH} = 8.5$  Hz, AR), 7.33 (t, 4H,  $J_{HH} = 7.0$  Hz, Ar), 7.61 (d, 2H,  $J_{HH} = 7.5$  Hz, Ar), 8.14 (s, 2H, Ar), 8.88 (s, 2H, HC=N);  $^{13}C\{H\}$  NMR (125 MHz, DMSO- $d_6$ ):  $\delta_C$  (ppm): 115.1 (2C), 116.0 (2C), 120.1 (2C), 120.2 (2C), 127.4 (2C), 134.1 (2C), 135.0 (2C), 142.2 (2C), 156.4 (2C-O) (AR), 165.2 (2C) (HC=N); IR:  $\nu_{max}/cm^{-1}$ :  $\nu_{(C-H)AR} = 3005$ ,  $\nu_{(C=N)} = 1600$ ,  $\nu_{(C-N)} = 1440$ ,  $\nu_{(C-O)} = 1192$ ,  $\nu_{(C-H)} = 752$ ,  $\nu_{(Ni-O)} = 543$ ,  $\nu_{(Ni-N)} = 455$ ; UV-Vis: (DMSO,  $10^{-3}M$ ):  $\lambda_{max}/nm$ : 255 ( $\pi \rightarrow \pi^*$ ), 373 ( $n \rightarrow \pi^*$ ), 472 (LMCT); CHN Anal. Calculated for  $C_{20}H_{14}N_2NiO_2$ ; C, 64.40; H, 3.78; N, 7.51, Ni = 15.73; found: C, 63.98; H, 3.67; N, 7.48, Ni, 15.69; HRMS-ESI,  $m/z$   $[M+H]^+$ : Calculated for  $C_{20}H_{14}N_2NiO_2 = 372.0420$ ; Found = 372.0087.

#### 2,2'-((1E, 1E)-(1,2-phenylenebis(azanylylidene))bis(methanylylidene))diphenolatezinc(II) (C2)

Yellow solid; Yield; (0.3643 g, 78%), mp:  $220^\circ C$ ;  $^1H$  NMR (500 MHz, DMSO- $d_6$ ):  $\delta_H$  (ppm): 6.52 (t, 2H,  $J_{HH} = 7.5$  Hz, Ar), 6.72 (d, 2H,  $J_{HH} = 8.5$  Hz, Ar), 7.26 (t, 2H,  $J_{HH} = 8.5$  Hz, Ar), 7.37-7.42 (m,

4H,  $J_{HH} = 7.0$  Hz, Ar), 7.89 (d, 2H,  $J_{HH} = 4.0$  Hz, Ar), 7.91 (d, 2H,  $J_{HH} = 4.0$  Hz, Ar), 9.01 (s, 2H, HC=N);  $^{13}\text{C}\{\text{H}\}$ NMR (125 MHz, DMSO- $d_6$ ):  $\delta_{\text{C}}$  (ppm): 112.9 (2C), 116.3 (2C), 119.3 (2C), 123.0 (2C), 127.1 (2C), 134.2 (2C), 136.1 (2C), 139.3 (2C), 162.7 (C-O) (AR); 172.2 (2C) (HC=N); IR:  $\nu_{\text{max}}/\text{cm}^{-1}$ :  $\nu_{(\text{C-H})\text{AR}} = 3005$ ,  $\nu_{(\text{C=N})} = 1612$ ,  $\nu_{(\text{C-N})} = 1314$ ,  $\nu_{(\text{C-O})} = 1182$ ,  $\nu_{(\text{C-H})} = 752$ ,  $\nu_{(\text{Ni-O})} = 532$ ,  $\nu_{(\text{Ni-N})} = 492$ ; UV-Vis: (DMSO,  $10^{-3}\text{M}$ ):  $\lambda_{\text{max}}/\text{nm}$ : 291 ( $\pi \rightarrow \pi^*$ ), 402 (LMCT); CHN Anal. Calculated for  $\text{C}_{20}\text{H}_{14}\text{N}_2\text{O}_2\text{Zn}$ ; C, 63.26; H, 3.72; N, 7.38, Zn, 17.22; found: C, 63.19; H, 3.69; N, 7.33, Zn, 17.18; HRMS-ESI,  $m/z$   $[\text{M}+\text{H}]^+$ : Calculated for  $\text{C}_{20}\text{H}_{14}\text{N}_2\text{Ni O}_2 = 379.0436$ ; Found = 379.1127.

**2,2-((1E,1'E)-(ethane-1,2-diylbis(azanyllidene))bis(methanylylidene))diphenolatenickel (II) (C3)**

Brown solid; Yield: (0.4418 g, 85%); mp: 205 °C;  $^1\text{H}$  NMR (500 MHz, DMSO- $d_6$ ):  $\delta_{\text{H}}$  (ppm): 3.42 (s, 4H, 2(CH<sub>2</sub>)), 6.52 (t, 2H,  $J_{HH} = 7.5$  Hz, Ar), 6.70 (d, 2H,  $J_{HH} = 8.5$  Hz, Ar), 7.18 (t, 2H,  $J_{HH} = 7.5$  Hz, Ar), 7.26 (d, 2H,  $J_{HH} = 7.0$  Hz, Ar), 7.89 (s, 2H, 2(HC=N));  $^{13}\text{C}\{\text{H}\}$ NMR (125 MHz, DMSO- $d_6$ ):  $\delta_{\text{C}}$  (ppm): 57.9 (2C), 114.2 (2C), 119.7 (2C), 120.2 (2C), 132.6 (2C), 133.4 (2C), 162.5 (C-O) (Ar), 163.9 (2C) (HC=N); IR:  $\nu_{\text{max}}/\text{cm}^{-1}$ :  $\nu_{(\text{C-H})\text{AR}} = 2947$ ,  $\nu_{(\text{C=N})} = 1624$ ,  $\nu_{(\text{C-N})} = 1323$ ,  $\nu_{(\text{C-O})} = 1122$ ,  $\nu_{(\text{C-H})} = 732$ ,  $\nu_{(\text{Ni-O})} = 594$ ,  $\nu_{(\text{Ni-N})} = 428$ ; UV-Vis: (DMSO,  $10^{-3}\text{M}$ ):  $\lambda_{\text{max}}/\text{nm}$ : 256 ( $\pi \rightarrow \pi^*$ ), 327 ( $n \rightarrow \pi^*$ ), 402 (LMCT); CHN Anal. Calculated for  $\text{C}_{16}\text{H}_{14}\text{N}_2\text{NiO}_2$ ; C, 59.13; H, 4.34; N, 8.62, Ni, 18.06; found: C, 59.10; H, 4.21; N, 8.58, Ni, 18.02; HRMS-ESI,  $m/z$   $[\text{M}+\text{H}]^+$ : Calculated for  $\text{C}_{16}\text{H}_{14}\text{N}_2\text{Ni O}_2 = 325.0498$ ; Found = 325.1034.

**2,2-((1E,1'E)-(ethane-1,2-diylbis(azanyllidene))bis(methanylylidene))diphenolatezinc(II) (C4)**

White solid; Yield: (0.4385 g, 82%); mp: 196 °C;  $^1\text{H}$  NMR (500 MHz, DMSO- $d_6$ ):  $\delta_{\text{H}}$  (ppm): 3.71 (s, 4H, 2(CH<sub>2</sub>)), 6.43 (t, 2H,  $J_{HH} = 7.5$  Hz, Ar), 6.63 (d, 2H,  $J_{HH} = 8.5$  Hz, Ar), 7.14 (t, 4H,  $J_{HH} = 7.5$  Hz, Ar), 8.41 (s, 2H, HC=N);  $^{13}\text{C}\{\text{H}\}$ NMR (125 MHz, DMSO- $d_6$ ):  $\delta_{\text{C}}$  (ppm): 55.6 (2C), 112.1 (2C), 119.2 (2C), 122.6 (2C), 132.7 (2C), 134.6 (2C), 167.9 (2(C-O)), (AR), 170.9 (2C) (HC=N); IR:  $\nu_{\text{max}}/\text{cm}^{-1}$ :  $\nu_{(\text{C-H})\text{AR}} = 2947$ ,  $\nu_{(\text{C=N})} = 1624$ ,  $\nu_{(\text{C-N})} = 1323$ ,  $\nu_{(\text{C-O})} = 1122$ ,  $\nu_{(\text{C-H})} = 752$ ,  $\nu_{(\text{Ni-O})} = 570$ ,  $\nu_{(\text{Ni-N})} = 459$ ; UV-Vis: (DMSO,  $10^{-3}\text{M}$ ):  $\lambda_{\text{max}}/\text{nm}$ : 274 ( $\pi \rightarrow \pi^*$ ), 352 ( $n \rightarrow \pi^*$ ); CHN Anal. Calculated for  $\text{C}_{16}\text{H}_{14}\text{N}_2\text{O}_2\text{Zn}$ ; C, 57.94; H, 4.25; N, 8.45, Zn, 19.71; found: C, 57.83; H, 4.23; N, 8.39, Zn, 19.67; HRMS-ESI,  $m/z$   $[\text{M}+\text{H}]^+$ : Calculated for  $\text{C}_{16}\text{H}_{14}\text{N}_2\text{O}_2\text{Zn} = 331.0436$ ; Found = 331.0951.

**Biological evaluations**

**Antioxidant studies**

The 2,2-diphenylpicrylhydrazyl (DPPH) assay was deployed to appraise the antioxidant activity of the free ligands and their complexes (Waziri *et al.*, 2022). In brief, a 0.1 mM stock solution of the DPPH radical was produced in absolute methanol, and 3 mL of the stock was added to 1 mL of solution of the complexes in

DMSO in a concentration range of (100–500)  $\mu\text{g. mL}^{-1}$ . The mixture was incubated in a dark room for 0.5 h, and absorbance was obtained using a spectrophotometer at a wavelength of 517 nm. Three duplicates of each measurement were made. The rate of radical activity of the compounds was estimated using the equation given below. Ascorbic acid was employed as a positive control.

$$\% \text{ SC} = [(A_0 - A_i) / A_0] \times 100$$

Where % SC = percentage scavenging,  $A_0$  = absorbance of the DPPH in methanol, and  $A_i$  = absorbance of the tested compounds with the DPPH in methanol.

### Xanthine oxidase inhibitory studies

To evaluate the xanthine oxidase inhibitory activity of the complexes, xanthine (X0626) and xanthine oxidase (X2252) were used following a modified literature procedure (Ikram *et al.*, 2019). DMSO was used to make a concentration range of (100–500)  $\mu\text{g}\cdot\text{mL}^{-1}$  complexes solutions, and 10  $\mu\text{L}$  of these solutions were added to 125  $\mu\text{L}$  of phosphate buffer (0.1  $\text{mol}\cdot\text{L}^{-1}$ , pH = 7.4). After that, 25  $\mu\text{L}$  of 0.003 units of xanthine dissolved in buffer and 25  $\mu\text{L}$  of 0.15  $\text{mmol}\cdot\text{L}^{-1}$  xanthine as the enzyme's substrate were added. The mixture was incubated for 10 min, and absorbance was measured using a UV-Vis spectrophotometer at 295 nm. The enzyme's substrate was added again to the reaction mixture with continued measurement of the absorbance for 0.5 h at an interval of 1 min. The percentage inhibition of the complexes comparative to allopurinol (positive control) was estimated using the relation.

Inhibitory (%) =  $100 - [(\text{absorbance of the compounds} \div \text{absorbance of the control}) \times 100]$ , and  $\text{IC}_{50}$  values were estimated.

### Computational studies

Using Gaussian 09 software, DFT calculations were performed on the complexes by first constructing them and then optimizing them at

the M06-2X/6-311G(d,p) level of theory (Frisch *et al.*, 2009). Optimization was done in the solvent (MeOH) phase using the polarizable continuum model (PCM) to describe solvation effects. In support of optimization, frequency calculations were used to verify whether the structures obtained were of minimum energies and produced the images in Fig. 1. Using the optimized structures, fchk files were created and used as input to perform quantum theory of atoms in molecules (QTAIM) analysis using multiwfn (Lu and Chen, 2012), vmd (Humphrey *et al.*, 1996) and gnuplot (Nylander *et al.*, 2008) software. Multiwfn software was used to prepare the files for non-covalent-interactions (NCI) as well as extract quantitative information about NCI, perform molecular electrostatic potentials (MEP), conceptual density functional theory (CDFT) and electron localization function (ELF) analyses. After the preparation of the files for NCI, they were then used as input to produce three-dimensional as well as the interacting paths using vmd software. Multiwfn software was also used to create input files for gnuplot software to produce two-dimensional NCI images.

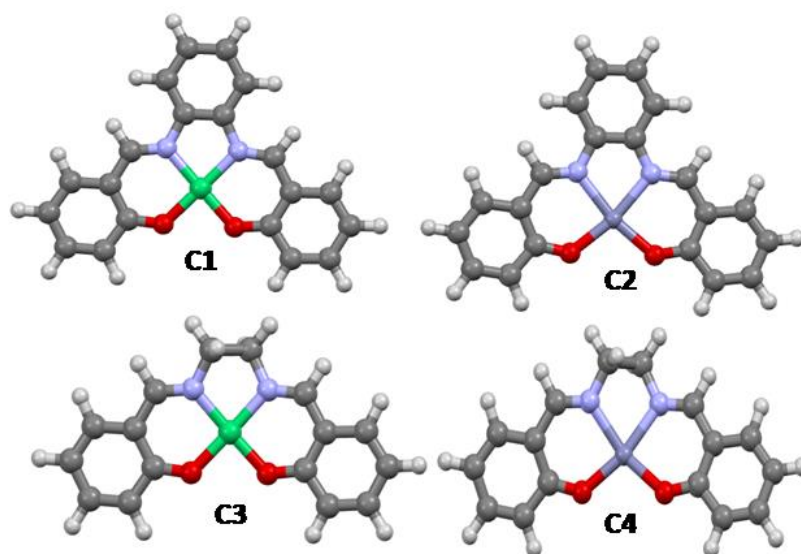


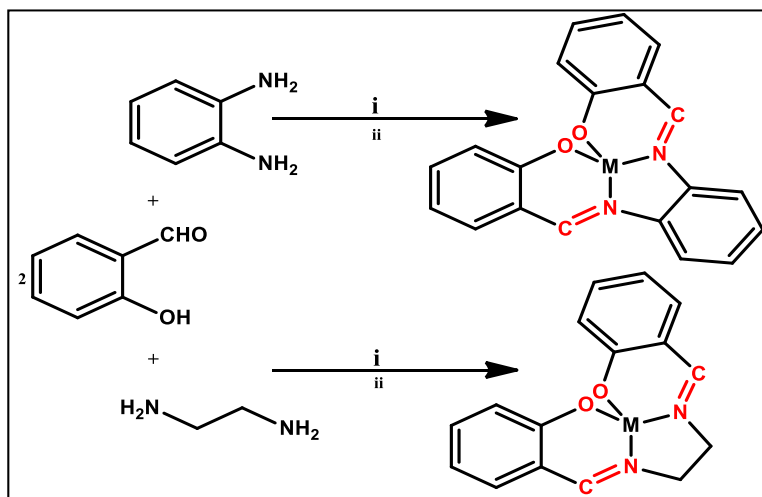
**Figure 1:** Optimized geometries of the complexes visualized with Mercury

## RESULTS AND DISCUSSION

### Synthesis and physico-chemical characteristics of the complexes

The complexes were synthesised using the template method, and the reaction pathway for the synthesis is presented in **scheme 1**. All the compounds were obtained in good yield (78–87%) and are of different colors, from white, yellow, to brown and dark brown, respectively. The elemental analyses of the compounds are in agreement with their stoichiometric composition and support their

proposed structures. They are found to be stable in some common polar and non-polar solvents such as methanol, ethanol, acetonitrile, chloroform, acetone, hexane, benzene, dimethyl sulfoxide, and dimethylformamide. The molar conductance measurement result for the complexes were found to be in the range of (2.3–4.8)  $\text{cm}^2 \cdot \text{mol}^{-1}$ , which is in accordance with those of non-electrolytic complexes reported in the literature (Ali *et al.*, 2013).



**Scheme 1:** Synthesis of the complexes, i =  $\text{NiCl}_2 \cdot 6\text{H}_2\text{O}$  or  $\text{Zn}(\text{NO}_3)_2 \cdot 6\text{H}_2\text{O}$ , ii =  $\text{CH}_3\text{OH}/\text{N}_2$ , rt, 6 h

### Nuclear magnetic resonance studies

NMR spectroscopy is a valuable tool for comprehending and validating molecular structures. It describes the chemical environment and atom interactions within a specific molecule. To validate the formation of the compounds,  $^1\text{H}$  and  $^{13}\text{C}\{\text{H}\}$ NMR spectra were obtained at ambient temperature using  $\text{DMSO-d}_6$  as a solvent on a 500 MHz and 125 MHz spectrometer, respectively, as shown in Figs. 2–9.

The  $^1\text{H}$  NMR spectra of the diamagnetic complexes shows the expected spectra, justifying the integrity of the complexes. The signal for the proton of the hydroxyl (OH) group was completely absent in all the spectra. This signal is expected to be downfield at

around 13.00 ppm in the uncoordinated ligand due to the deshielding effect arising from the electronegative oxygen atom (Dilmen Portakal *et al.*, 2022). The disappearance of this signal in all the complexes is due to the deprotonation of the phenolic proton and formation of bond between the metal and oxygen atom of the phenolate group. Similarly, the signal for the azomethine (HC=N) proton in all the complexes appears at 8.88, 9.01, 7.89, and 8.41 ppm in the spectra of C1, C2, C3, and C4, respectively. This signals are expected to appear in the spectra of uncoordinated ligands (Dilmen *et al.*, 2022) around 8.5–8.7 ppm. The shifts to the downfield in C1 and C2, and to the upfield in C3 and C4, are due to the participation of

nitrogen atom from the azomethine in the formation of bonding with metal ions through the lone pair of electrons, resulting to M-N bond (Dilmen *et al.*, 2022). Aromatic protons were observed in the spectra of C1, C2, C3, and C4 at 7.68-8.14, 6.52-7.91, 6.52-7.26, and 6.43-7.14 ppm, respectively. As can be seen from the spectra, the position, shape, and integrating values of the aromatic proton signals were affected by the relaxation time, rate of exchange, and the concentration of the sample in the solvent used. This can be

explained further on the basis that the amount of water is high, as seen from the water peak at 3.34 ppm.

The  $^{13}\text{C}\{\text{H}\}$ NMR spectra of all the complexes shows characteristic signals that account for the number of carbon atoms in the respective compounds. The peaks at 165.2, 172.2, 163.9, and 170.9 in the spectra of C1, C2, C3, and C4, respectively, due to the azomethine carbon atoms, affirmed the existence of Schiff base in the complexes (Dilmen *et al.*, 2022).

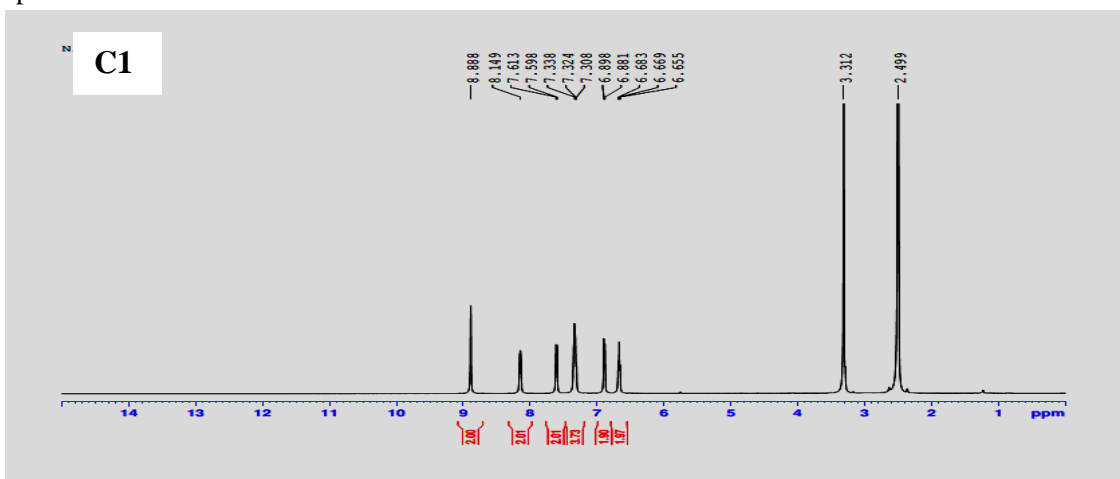


**Figure 2:**  $^1\text{H}$  NMR spectrum of C1 (500 MHz, DMSO- $\text{d}_6$ )

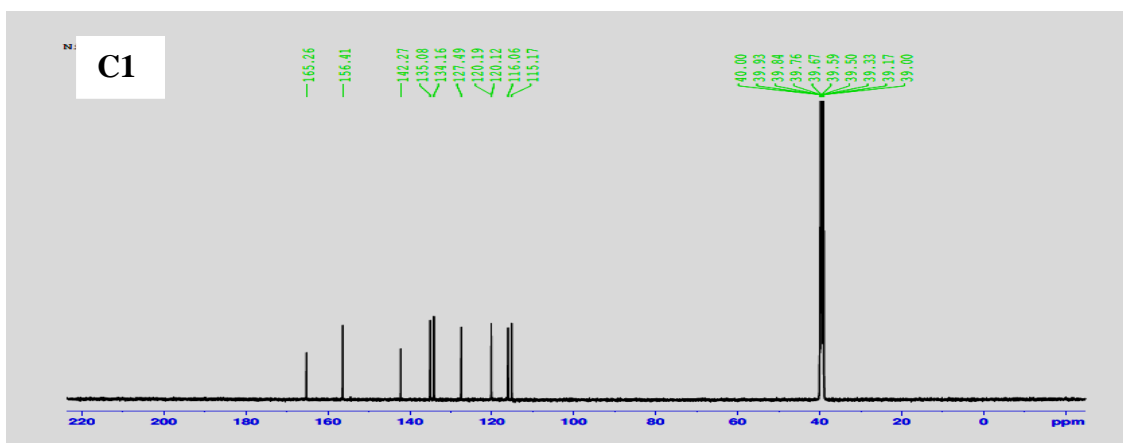


**Figure 3:**  $^{13}\text{C}\{\text{H}\}$ NMR spectrum of C1 (125 MHz, DMSO- $\text{d}_6$ )



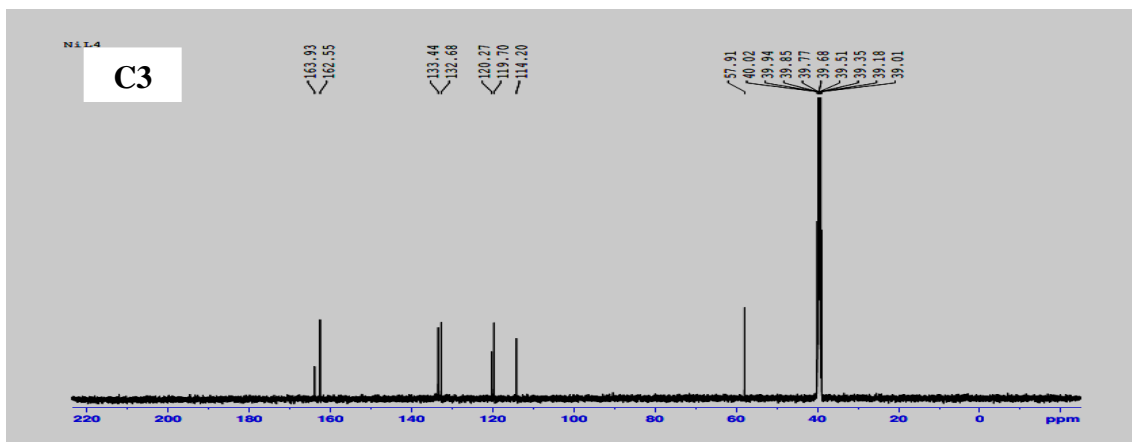


Figure 7:  $^{13}\text{C}\{\text{H}\}$ NMR spectrum of C3 (125 MHz,  $\text{DMSO-d}_6$ )

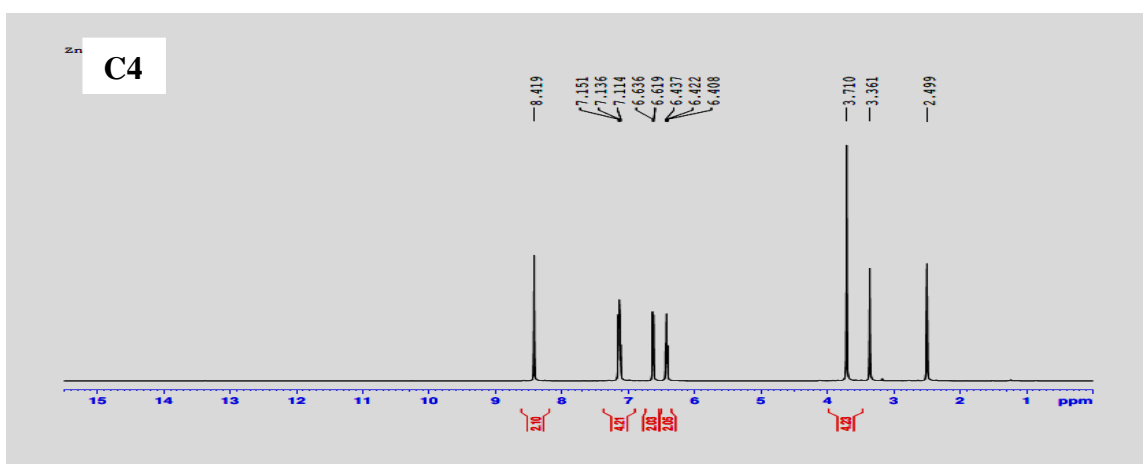


Figure 8:  $^1\text{H}$ NMR spectrum of C4 (500 MHz,  $\text{DMSO-d}_6$ )

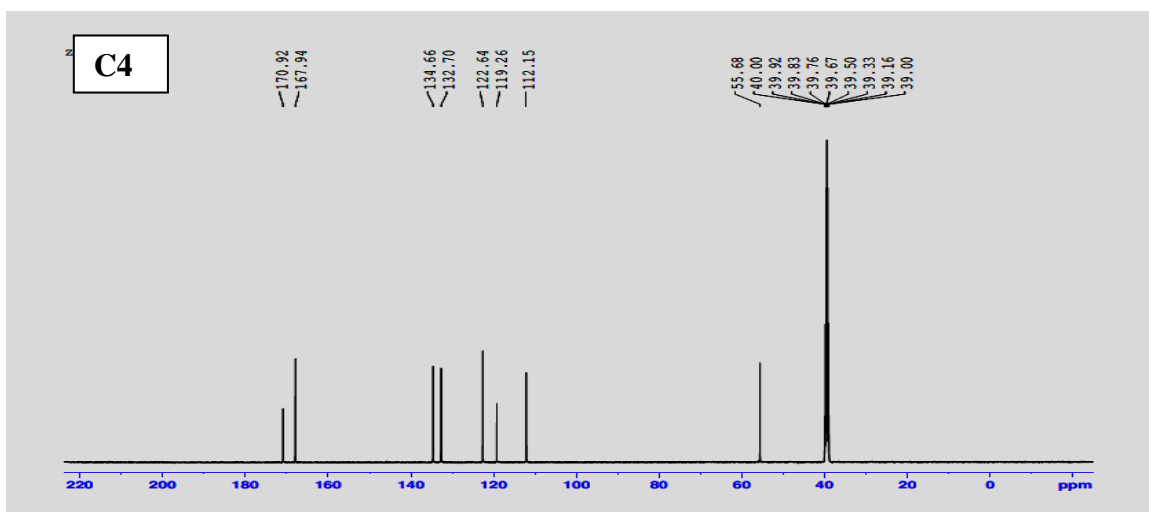


Figure 9:  $^{13}\text{C}\{\text{H}\}$ NMR spectrum of C4 (125 MHz,  $\text{DMSO-d}_6$ )

### Infrared spectral studies

The complexes' IR spectra were investigated in the  $4000\text{-}400\text{ cm}^{-1}$  region, and the spectra

are shown in Fig. 10. The C=N stretching vibration bands are the most prominent feature noticed in these spectra. They were observed

at 1600, 1612, 1624, and 1624  $\text{cm}^{-1}$ , for C1, C2, C3, and C4, respectively. In uncoordinated ligands, this band is typically seen at 1690-1640  $\text{cm}^{-1}$  (Milbeo *et al.*, 2021). The participation of the nitrogen atom in the emergence of M-N bonds, and enfeebling of C=N bonds due to the donation of electron pair from nitrogen atom to the vacant orbital of the metal ion are responsible for the shifts to a lower wave numbers of this bands in the complexes (Milbeo *et al.*, 2021). Likewise, the appearance of a weak/medium bands at 3005–

2947  $\text{cm}^{-1}$  is due to the C-H stretching vibration of the aromatic moieties. Furthermore, 1192  $\text{cm}^{-1}$  C1, 1182  $\text{cm}^{-1}$  C2, and 1122  $\text{cm}^{-1}$  (C3 and C4) C-O stretching vibrations confirm the existence of phenolate groups in the compounds (Milbeo *et al.*, 2021). The appearance of weak intensity bands at 594-532  $\text{cm}^{-1}$  and 492-428  $\text{cm}^{-1}$ , arising from the formation of M-O and M-N bonds, respectively, provided additional support for the complexes' formation.

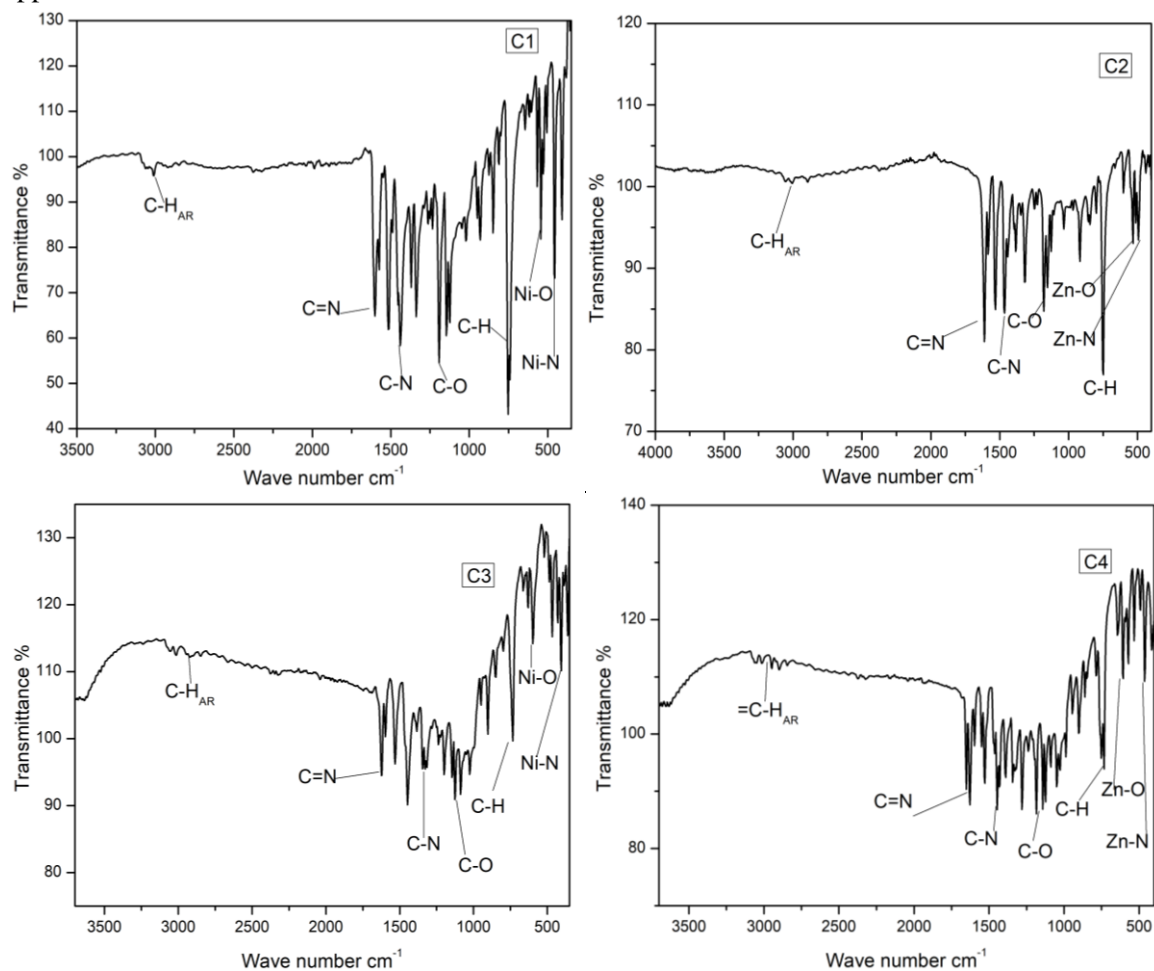


**Figure 10:** IR spectra of the complexes

### UV-Visible absorption studies

The electronic absorption spectra of the complexes were recorded in dimethyl sulfoxide as the solvent at room temperature in the region of 800-200 nm at a concentration of  $10^{-3}$  M, and the spectra are shown in Fig. 11.

In the spectra, the complexes showed absorption bands in the 255-472 nm range. C1 has absorption bands at 255, 302, 373, and 472 nm, C2 has bands at 291 and 390 nm, C3 has bands at 256, 327, and 402 nm, and C4 has bands at 274 and 352 nm. The bands

appearing at 255–291 nm can be assigned to the  $\pi \rightarrow \pi^*$  transition due to the aromatic moieties of the ligands (Mahmoud *et al.*, 2020). The bands at 327–390 nm are associated with the azomethine (HC=N)  $n \rightarrow \pi^*$

transition (Mahmoud *et al.*, 2020). Furthermore, the absorption bands at the lower energy regions of 400–472 nm are attributed to the ligands to metal charge transfer (LMCT) transition (Mahmoud *et al.*, 2020).

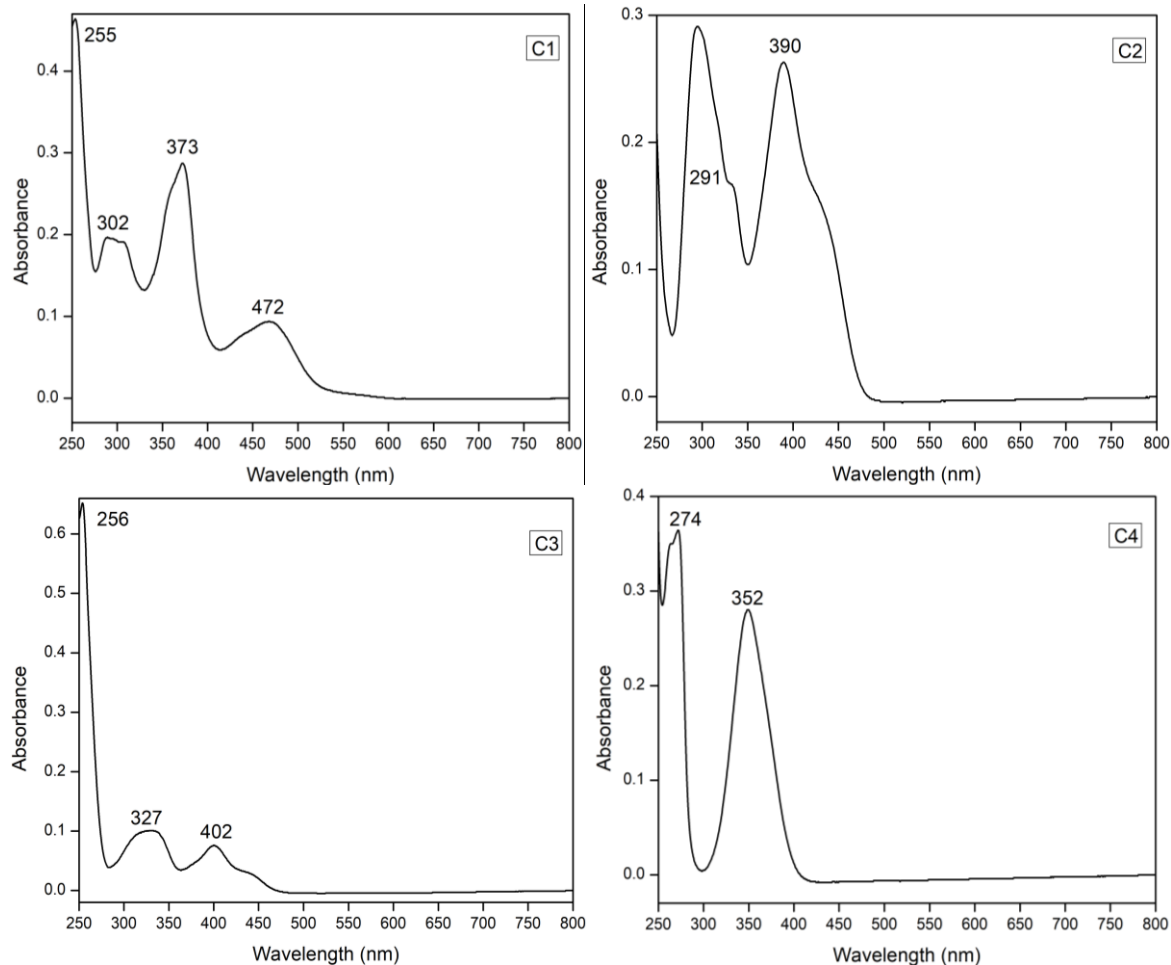


**Figure 11:** UV-Visible absorption spectra of the complexes

#### Powder X-ray diffraction (PXRD) analysis

Several attempts were made, but single crystals suitable for single crystal X-ray diffraction (SCXRD) data collection were not obtained. PXRD was used to examine the

micro-crystalline nature and aggregation of the complexes. Fig. 12 depicts the diffraction patterns obtained from the analysis. The PXDR spectra revealed that the complexes are polycrystalline.

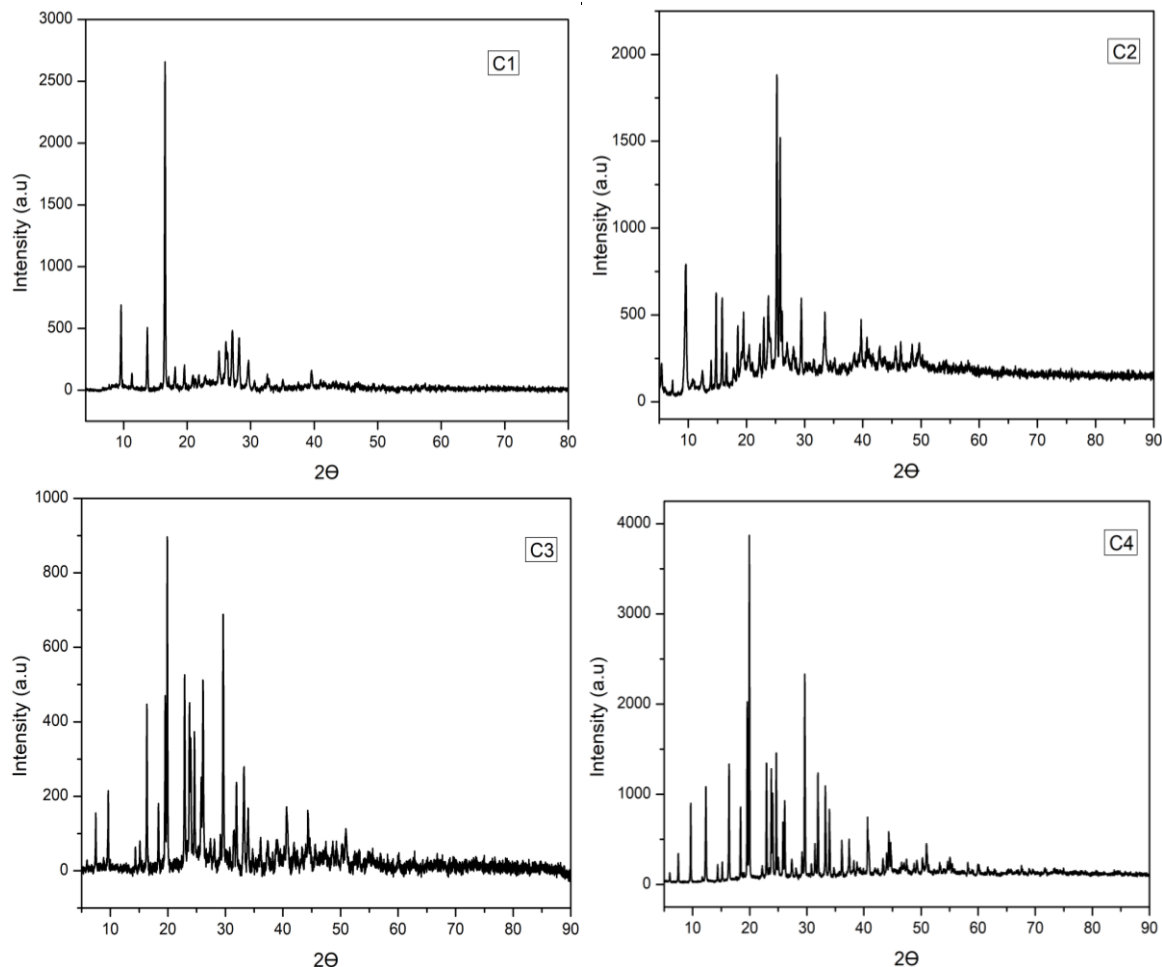
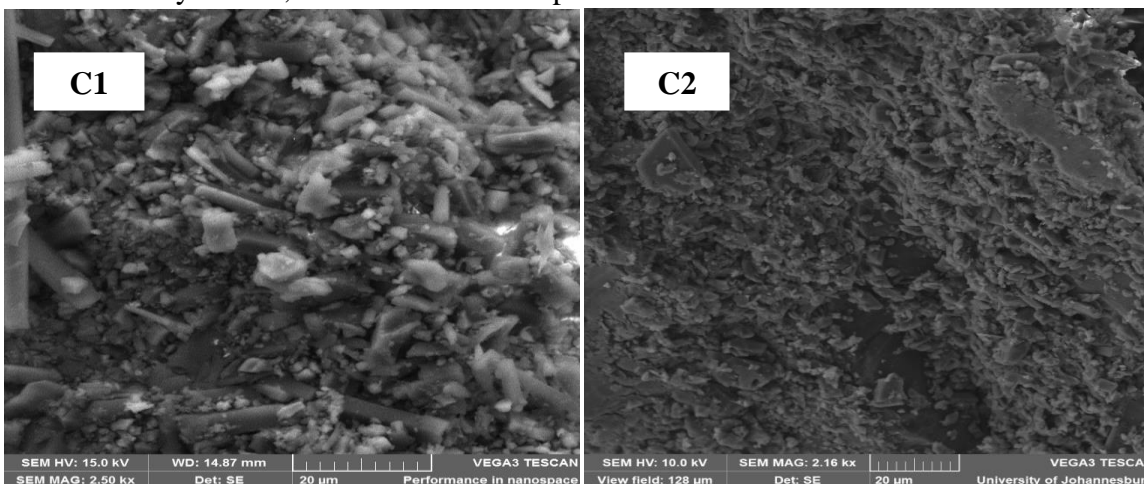
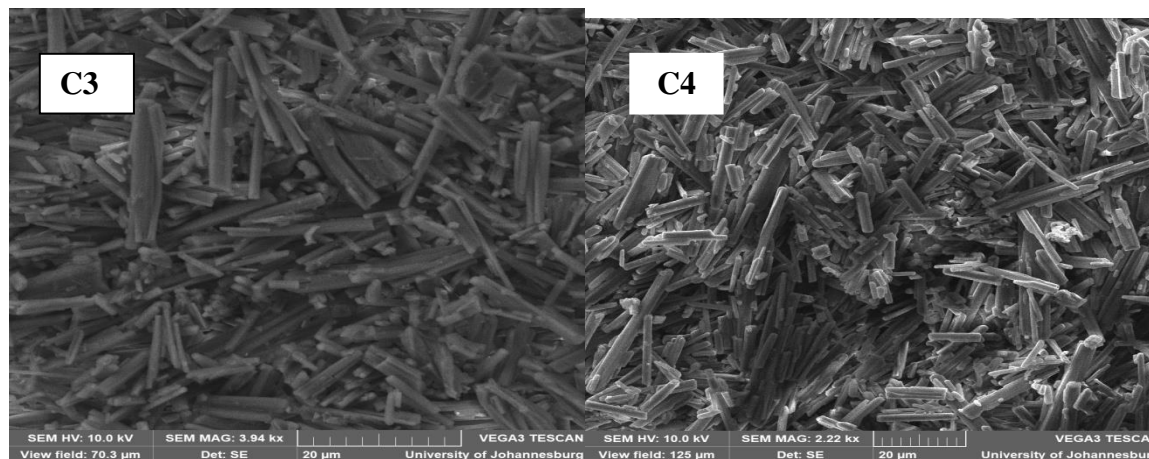


Figure 12: Powder x-ray diffraction spectra of the complexes

**Scanning electron microscopy (SEM) analysis**

SEM analysis was used to investigate the surface morphology of the complexes. A SEM image of the complexes is shown in Fig. 13. C1 and C2 have agglomerative wide-fine block-like surfaces, whereas C3 and C4 have well-defined rod-like surfaces. As a result, C1, C3, and C4 are crystalline, whereas C2 is amorphous.



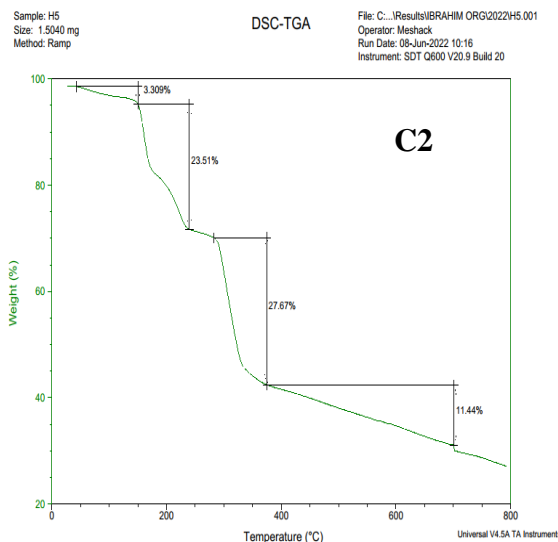
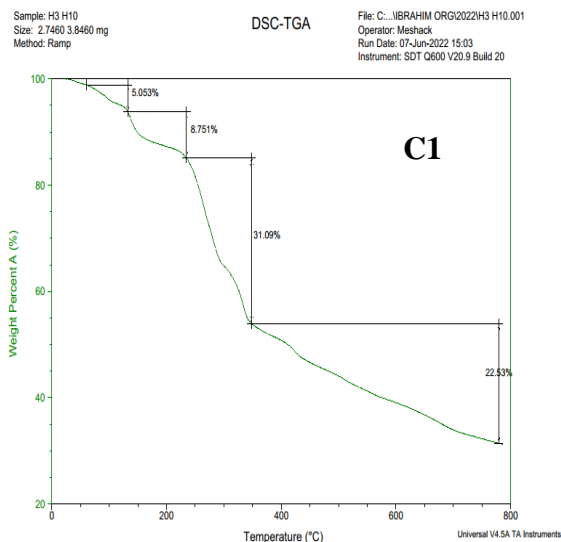


**Figure 13:** SEM images of the complexes

**Thermogravimetric analysis (TGA)**

The complexes were subjected to thermogravimetric analysis to get information regarding their thermal stability at a temperature range of 25–800 °C, and the thermograms are given in Fig. 14. The

thermograms showed various decomposition steps within the complexes. These decomposition steps represent moisture loss, organic moiety (ligand) loss, and formation metal oxide.



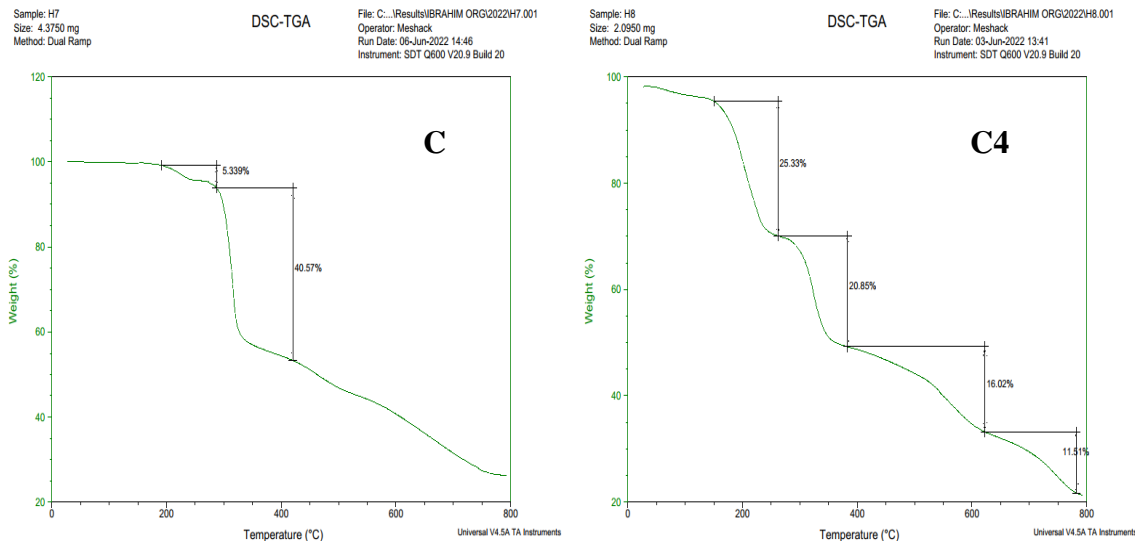


**Figure 14:** Thermograms of the complexes

### Structure of the complexes

On basis of the characterization performed on the complexes, it is established that the ligand coordinated to the metal ion via oxygen and nitrogen atoms of the phenolate and

azomethine groups respectively giving rise to perfect square planar and distorted square planar geometries for Ni(II) and Zn(II) complexes, respectively. The structures of the complexes are presented in Fig. 15.

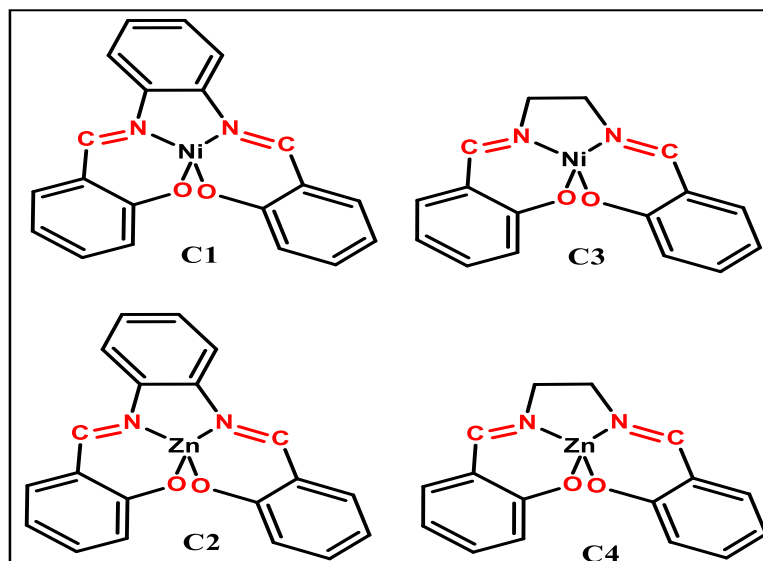


**Figure 15:** Structures of the complexes

### Biological Evaluations

#### Antioxidant studies

The radical scavenging activity of the complexes was evaluated based on their ability to quench free radicals and compared with ascorbic acid as a positive control using the DPPH assay. The percentage of DPPH

scavenging activity and  $IC_{50}$  of the test compounds and control are presented in Table 1 and Fig. 16–17. Based on the results, the complexes' ability to scavenge radicals is concentration dependent. All of the complexes were found to have less radical scavenging activity than ascorbic acid. At a concentration

of 500  $\mu\text{g.mL}^{-1}$ , C3 demonstrated slightly higher radical scavenging activity than ascorbic acid. The absence of phenolic protons, which could easily be donated to stabilize the DPPH radicals, could explain the complexes' lack of radical scavenging activity when compared to ascorbic acid. During the coordination process, these protons were deprotonated, resulting in a phenolate oxygen atom coordinated to the metal ions. Table 1 show the  $\text{IC}_{50}$  and  $\text{pIC}_{50}$  values for the complexes and ascorbic acid. The higher the  $\text{IC}_{50}$  value as a radical eliminator, the lower

the radical scavenging activity of a compound, and the higher the  $\text{pIC}_{50}$  value, the stronger the radical scavenging activity of the compound.  $\text{IC}_{50}$  is the concentration required for 50% radical scavenging, and  $\text{pIC}_{50}$  is the potency of the radical scavenger. The complexes' and ascorbic acid's  $\text{IC}_{50}$  and  $\text{pIC}_{50}$  values are 342.5, 574.7, 316.5, 378.8, and 301.2  $\mu\text{g.mL}^{-1}$ , and -2.53, -2.74, -2.50, -2.58, and -2.48  $\mu\text{g.mL}^{-1}$ , respectively. Based on the  $\text{IC}_{50}$  and  $\text{pIC}_{50}$  values, it is possible to conclude that the complexes' radical scavenging activity is on the order of  $\text{C3} > \text{C1} > \text{C4} > \text{C2}$

**Table 1:** Percentage of DPPH radical scavenging activity of the complexes and the control

Conc. ( $\mu\text{g.mL}^{-1}$ )	Radical scavenging activity (%)				
	C1	C2	C3	C4	AA
100	17	15	18	13	21
200	33	19	36	32	41
300	49	26	48	48	54
400	58	31	66	52	68
500	69	45	77	57	76
$\text{IC}_{50}$	<b>342.5</b>	<b>574.7</b>	<b>316.5</b>	<b>378.8</b>	<b>301.2</b>
$\text{pIC}_{50}$	<b>-2.53</b>	<b>-2.74</b>	<b>-2.50</b>	<b>-2.58</b>	<b>-2.48</b>

AA = Ascorbic acid

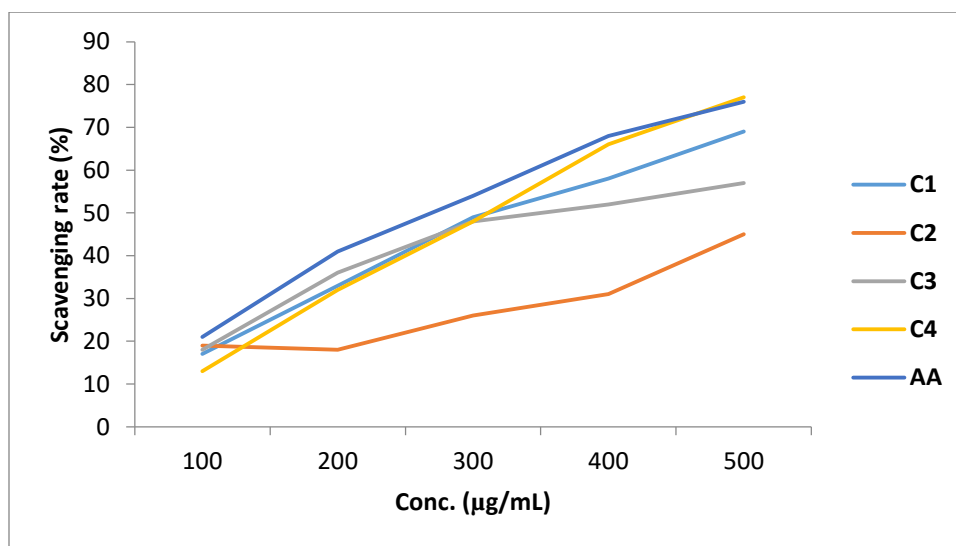


**Figure 16:** Plot of the DPPH scavenging activity of the complexes and the ascorbic acid

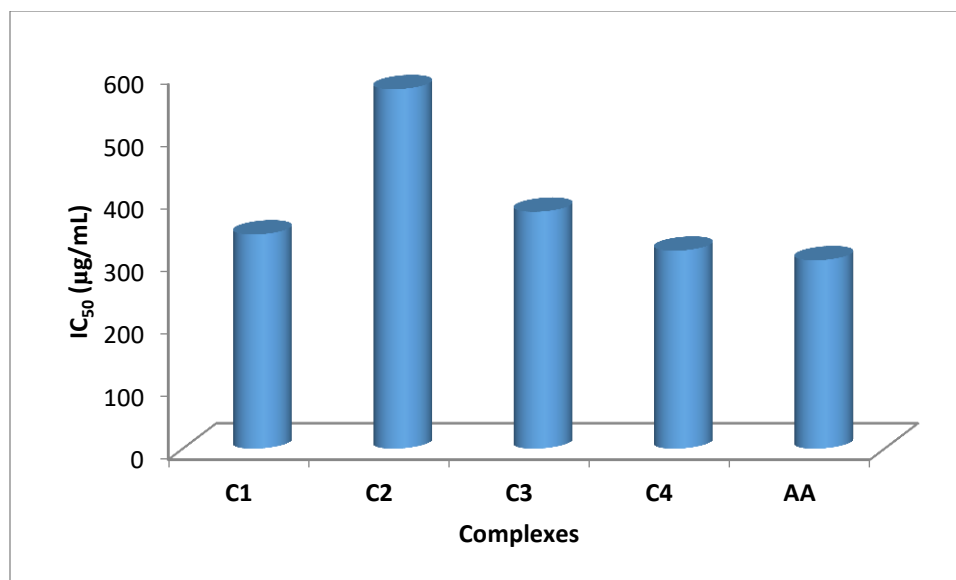


**Figure 17:** Plot of IC<sub>50</sub> values of the complexes and the control on DPPH radical

#### Xanthine oxidase inhibitory activities studies

Xanthine oxidase is an enzyme that facilitates the oxidation process for the conversion of hypoxanthine to xanthine and subsequently to uric acid and hydrogen peroxide on further oxidation (Al-Shehri *et al.*, 2020). It take part in the production excess uric acid in the body system, and resulted in hyperuricemia in the joint and other sites of the body. It is one of the key players in a number of lungs, and heart diseases, including type II diabetics and obesity (Tamta *et al.*, 2006). Most of the xanthine oxidase inhibitors commonly in used are associated with some side effects and

toxicities, which necessitate a search for new essential inhibitors.

The xanthine oxidase inhibitory activity of the complexes and the control is shown in Table 2. From the results obtained, it can be seen that all the complexes failed to inhibit xanthine oxidase at all the concentration tested compared to the control. However, C1 and C3 shows slight inhibition at high concentration but not commensurate with the control. In addition, the IC<sub>50</sub> value for C1, C3 and the control were found to be 862, 649 and 206 µg.mL<sup>-1</sup>, respectively. This further affirmed the non-inhibitory of activity of the synthesised complexes against the xanthine oxidase.

**Table 2:** Xanthine inhibitory activity of the complexes and the control

Conc. (µg.mL <sup>-1</sup> )	Inhibitory activity (%)				
	C1	C2	C3	C4	AI
100	-	-	-	-	65±0.08
200	-	-	-	-	78±0.7
300	-	-	-	-	86±0.04
400	26±0.81	-	33±0.23	-	92±0.1
500	43±0.14	-	59±0.25	-	97.3±0.9
IC <sub>50</sub>	<b>862</b>	-	<b>649</b>	-	<b>206</b>

AI = Allopurinol

### Computational studies

#### Non-covalent-interactions (NCI)

Non-covalent-interactions (NCI) revealed interactions that stabilize compounds, which include hydrogen bonding, and van der Waals attractive and repulsive forces. NCI can be identified by multi-coloured isosurfaces, which can be green and red sheets (van der Waals attractive and repulsive interactions), red pill shape in the centre of aromatic rings (closure of the benzene ring), blue disk shape (hydrogen bonding), and red and green folded sheets (multicentric building up of electron density, which causes stabilization and destabilization of the chelate ring) (Chaudret *et al.*, 2014; Trzesowska *et al.*, 2005). No hydrogen bonding was observed in the complexes. C-H $\cdots$ H van der Waals contact forces are also observed in C1 and C2 where their interacting paths are indicated in Fig. 18. N $\cdots$ O, and N $\cdots$ N repulsive interactions are observed in C1 and C3. The multicentric building up of electron density that stabilizes and destabilizes the chelate ring is observed in the Zn complexes but not in the Ni complexes.

As a red colour is predominantly observed, destabilization dominates in these complexes. Previous studies of Ni and Zn complexes have shown a tendency towards square planar for the former, and octahedral and square pyramidal geometries for the latter (Sarıkavaklı *et al.*, 2022). Two-dimensional NCI can be identified by observing well defined troughs for reduced density gradients (RDG) of *close to zero* for the loci in space. An index  $\rho$  is used to measure the strength of these interactions where the highest  $\rho$  reveals the strongest interaction. As was observed in Fig. 19 for C1 and C2, van der Waals attractive forces are also observed in the two-dimensional plots. We observe a stronger C-H $\cdots$ H interaction in C2 than in C1 (Table 3). Similarly, a weaker Zn-O and Zn-N interaction than Ni-O and Ni-N interaction were observed. This provides a plausible explanation for the red and blue folded sheet that was observed in Fig. 20, and why the red colour that represents destabilization dominates.

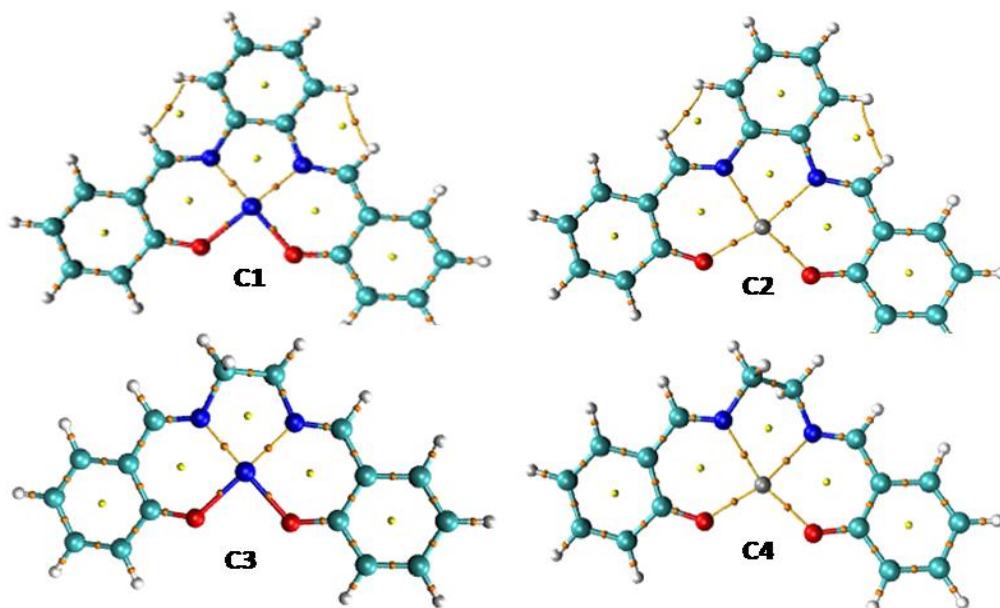


**Figure 18:** Non-covalent interacting paths for the complexes

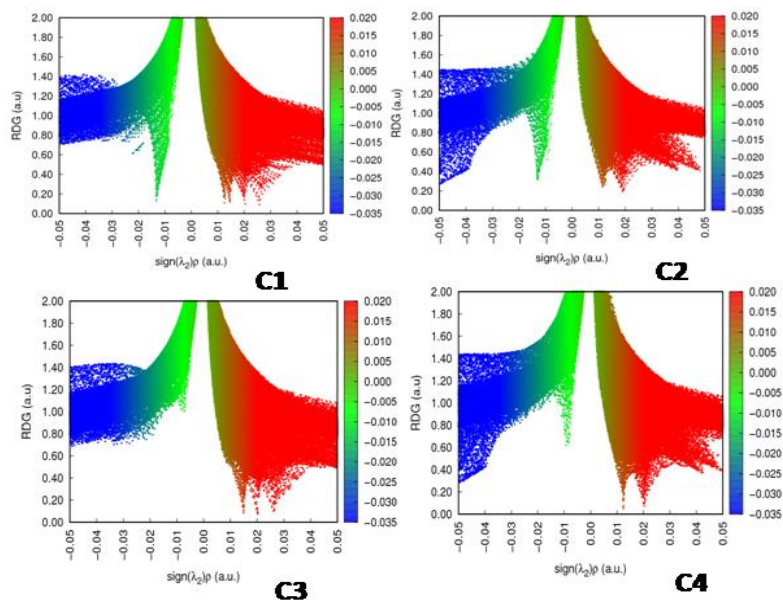


**Figure 19:** RDG scatter map for electron density distribution among the complexes

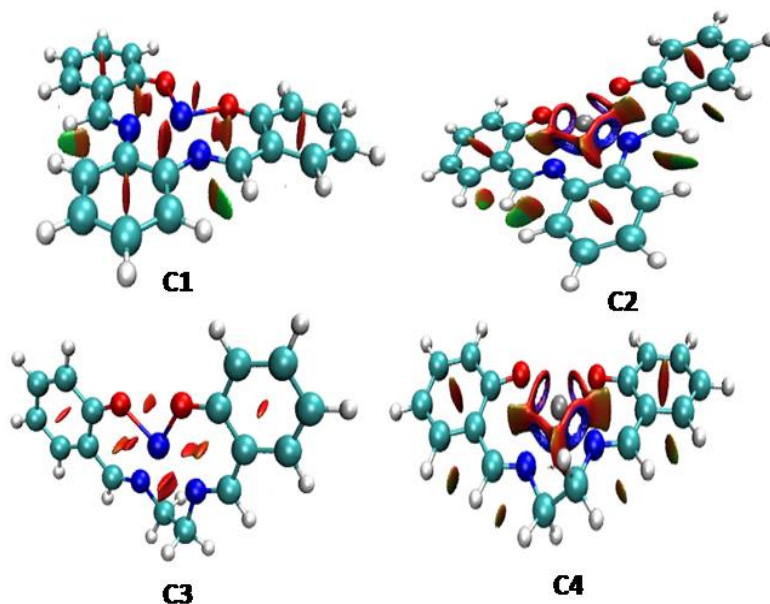


**Figure 20:** Three-dimensional non-covalent-interactions in the complexes

**Table 3:** Electron densities ( $\rho$ ) for the reduced density gradient (RDG) in each compound

Interaction	$-\lambda(\rho)$ C1	$-\lambda(\rho)$ C2	$-\lambda(\rho)$ C3	$-\lambda(\rho)$ C4
C-H $\cdots$ H	-0.0135	-0.0146		
Ni-O	-0.0922		-0.281	
Ni-N	-0.0967		-0.0981	
Zn-O		-0.0713		-0.0717
Zn-N		-0.0589		-0.0599

### Molecular electrostatic potentials (MEP)

Molecular electrostatic potential (MEP) is a chemical descriptor that studies the reactive sites on compounds based on differences in electro negativities that it detects around these sites. In doing so, this descriptor then reveals an electron density map with colours that includes blue, green, yellow, orange, and red (Fig. 21). As the electron densities reduces in the order blue>green>yellow>orange>red, a blue colour is highly indicative of a nucleophilic attack, while a red colour represents an electrophilic attack (Kostova *et al.*, 2005). As shown in Fig. 21, electrons are mainly concentrated around the Ni core, and

become less concentrated as you move away from this core. The concentrations of electron around Ni core in C1 and C3 is due to the electron rich  $d^8$  metal centre. In the Zn complexes, electrons are concentrated all around these complexes. When assigning the atomic codes on the donor atoms (Fig. 22), the quantitative measurements for these donor atoms could be identified (Table 4). These measurements show a higher concentration of electrons around the donor atoms in the Zn complexes than the Ni complexes, other than the oxygen donor atoms in C3 and C4. These measurements verify the earlier observations.

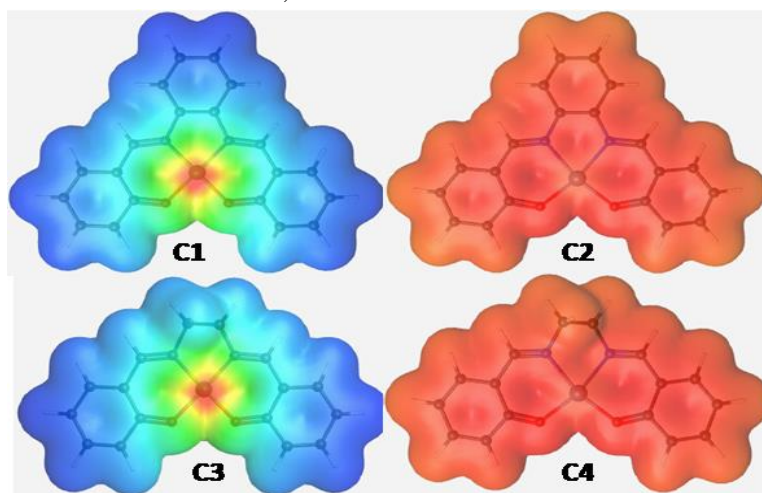


**Figure 21:** MEP map that represents the variation in electron densities around atomic sites

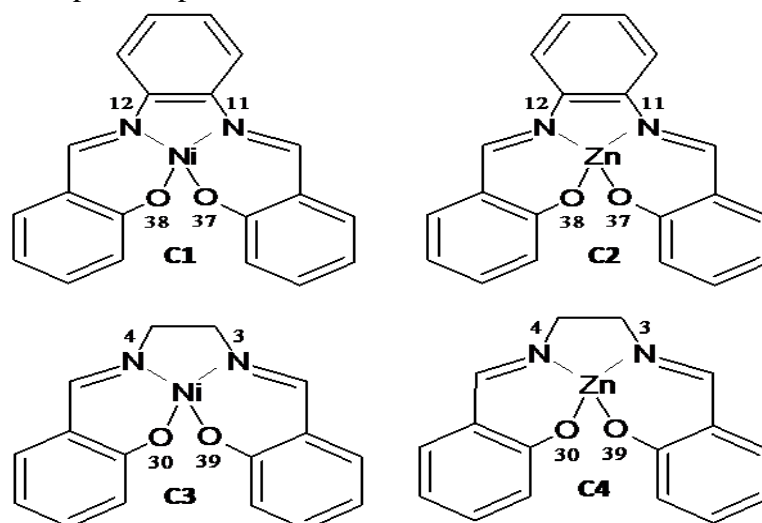


**Figure 22:** Atomic numbering for the donor atoms of the complexes

**Table 4:** MEP values ( $-1 \times 10^{-3}$ ) around the donor atoms of the complexes

Atom	C1	C2	C3	C4
N3			97.4	150
N4			97.4	150
N11	92.8	200		
N12	92.8	200		
O29			427	426
O30			427	426
O37	363	435		
O38	363	435		

### Conceptual density functional theory (CDFT)

Conceptual density functional theory is an alternative chemical descriptor to MEP. However, unlike MEP that only measures reactive sites that probes electrophilic and nucleophilic attacks, CDFT can also detect sites where radical attacks can occur as well as measuring chemical potential, ionization potential ( $IP$ ), electron affinity ( $EA$ ), electrophilicity index ( $\omega$ ), nucleophilicity index ( $N$ ), chemical hardness ( $\eta$ ), global softness ( $\delta$ ), electro negativity ( $\chi$ ), and energy differences (Table 5). As radical attacks are an indicator of a reactive site that acts as a broom that sweeps up reactive oxygen species (ROS) to inactivate them, identifying these sites can be quite useful for structure-activity relationships in molecular docking analyses. As the resistance of an atom to charge transfer (CT) can be measured by  $\eta$  (Chattaraj and Giri, 2009; Roy *et al.*, 1998), the ability of an atom or a group of atoms to receive electrons is measured by  $\delta$  (Chattaraj and Roy, 2007). Stabilization energies can then be predicted using the parameter  $\omega$ , which can be useful in estimating biological activities (Parr *et al.*, 1999; Zhan *et al.*, 2003).  $N$  can be used to measure the electrophilic and nucleophilic behavior of an organic molecule (Pahuja *et al.*, 2022).  $EA$  can be used to measure the electron accepting power of an accepting molecule when releasing energy as its “jumps” from the highest occupied molecular orbital (HOMO) to the lowest unoccupied molecular orbital (LUMO) (Fig. 2) (Chattaraj and Giri, 2009).

The  $IP$  can be used to remove an electron from the HOMO, which is also in indication of the electron donating power of a compound (Domingo and Pérez, 2011). The stability of a compound is usually determined by the HOMO-LUMO energy gap, with lower gaps indicating more stable compounds (Lewis *et al.*, 1994). Earlier studies suggested that an electron that occupies the HOMO level will automatically be excited to the LUMO level, but a recent study by Bulat *et al* revealed that the electron’s position in atomic space and the contour of the molecule also play a role in excitations (Esrafil *et al.*, 2014). However, the role that HOMO-LUMO energy gaps play in electron excitations is still generally accepted (Al-Rabiah *et al.*, 2017). The complexes with two aromatic rings display greater stability, lower  $IP$ , lower  $EA$ , lower  $\chi$ , higher  $\eta$ , lower  $\delta$ , lower  $\omega$ , higher  $N$  and higher  $\mu$ . Due to this; the additional aromatic ring would be expected to enhance biological activities. As a comparison between the Ni and Zn complexes display a similar pattern, the latter would also be expected to show higher biological activities than the former. These results correlate well with biological evaluation result. Although electrons are more localized in the Zn complexes, comparing C3 to C4 does not show any significant difference in localization of electrons other than a small portion of electrons being localized across the Ni centre but not across the Zn centre. Upon excitation, these electrons are delocalized away from the metal centre other than in C3.

**Table 5:** Comparisons of the energies HOMO-LUMO, energy gaps and Ionization Potentials for the complexes

<b>Compound</b>	<b>HOMO (eV)</b>	<b>LUMO (eV)</b>	<b><math>\Delta E</math> (eV)</b>	<b>Ionization Potential (eV)</b>	<b>Electron Affinity (A)</b>	<b>Electro-negativity (<math>\chi</math>)</b>	<b>Hardness (<math>\eta</math>)</b>	<b>Softness (<math>\delta</math>) (<math>1 \times 10^{-2}</math>)</b>	<b>Electrophilicity index (<math>\omega</math>)</b>	<b>Nucleophilicity index (<math>N</math>)</b>	<b>Chemical Potential (<math>\mu</math>) (eV)</b>
<b>C1</b>	-7.107	-1.637	5.470	6.501	0.484	3.493	6.016	1.662	1.014	3.924	-3.493
<b>C2</b>	-6.896	-1.482	5.415	6.749	0.741	3.745	6.008	1.665	1.167	3.676	-3.745
<b>C3</b>	-6.951	-0.973	5.977	6.364	0.289	3.326	6.075	1.646	0.911	4.130	-3.326
<b>C4</b>	-6.925	-0.795	6.130	6.642	0.094	3.368	6.548	1.527	0.866	3.853	-3.368

Measurements of local quantities on atomic sites can be performed by CDFT using a descriptor called the Fukui Function, which

$$f(\vec{r}) = \frac{\partial \rho}{\partial N} v(\vec{r}) = \left( \frac{\delta \mu}{\delta v \vec{r}} \right) N \dots\dots\dots 1$$

The condensed Fukui Functions ( $f$ ,  $f^+$  and  $f^\theta$ ) and charge density difference (CDD) are

$$f^+(r) = q_r(N+1) - q_r(N) \dots\dots\dots 2$$

**for a nucleophilic attack**

$$f^\theta(r) = q_r(N+1) - q_r(N-1) \dots\dots\dots 3$$

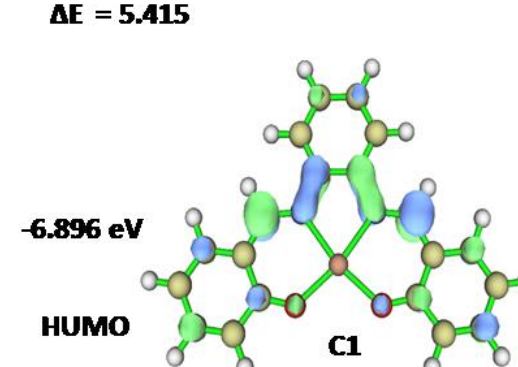
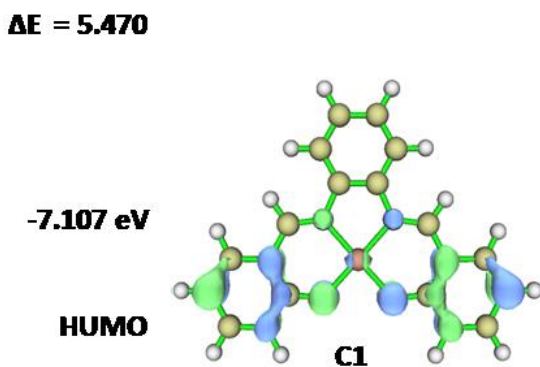
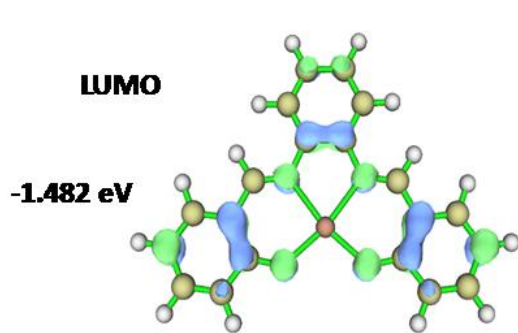
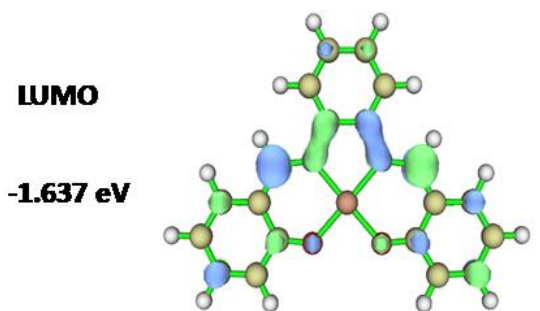
**for a radical attack**

The charge density difference (CCD) is the difference between  $f^+(\vec{r})$  and  $f^\theta(\vec{r})$  (Al-Rabiah *et al.*, 2017). As the quantitative values for the reactivity agrees with the quantitative values for MEP analyses, it was worthwhile to observe the radical attacks. Throughout the complexes, a higher probability for a radical attack on the oxygen atoms will occur than the nitrogen atoms. This is quite surprising since

relates the reactivity/selectivity of a specific site on a molecule. It is defined as follows

depicted in Table 6. The Fukui Function can be calculated using the following equations

the nitrogen atoms forms part of an imine moiety that usually display high biological activities. The complexes with less aromatic rings display higher probabilities for radical attacks. In general, the Zn complexes seem to display lower probabilities for radical attacks, but this is not the case on the nitrogen atom when comparing C3 to C4.



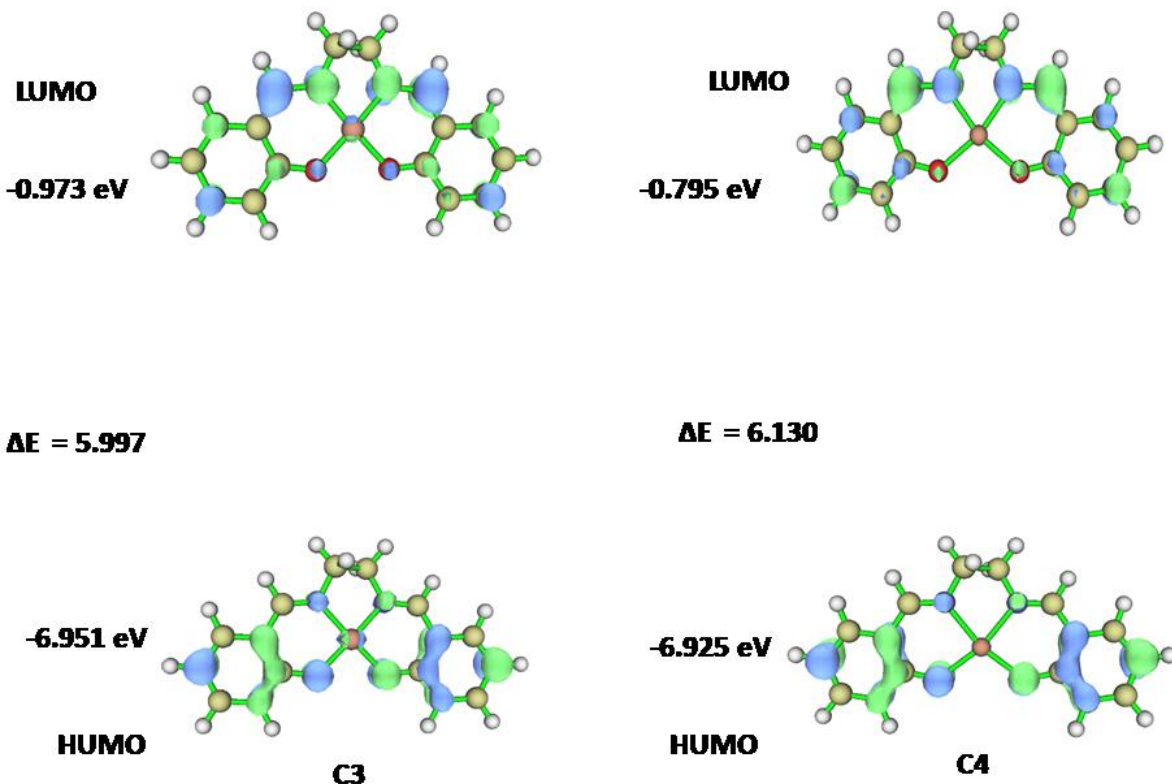


Fig. 23: The molecular orbital diagrams of HOMO and LUMO of the complexes

Table 6: Conceptual density functional theory parameters for the complexes

C1				
Atom	$f^-$	$f^+$	$f^0$	CDD
N11	0.0186	0.0316	0.0251	0.0130
N12	0.0186	0.0316	0.0251	0.0130
O37	0.0503	0.0369	0.0436	-0.0134
O38	0.0503	0.0369	0.0436	-0.0134
C2				
N11	0.0180	0.0195	0.0188	0.0015
N12	0.0180	0.0195	0.0188	0.0015
O37	0.0567	0.0247	0.0407	-0.0319
O38	0.0567	0.0247	0.0407	-0.0319
C3				
N3	0.0182	0.0270	0.0226	0.0088
N4	0.0182	0.0270	0.0226	0.0088
O29	0.0561	0.0375	0.0468	-0.0185
O30	0.0561	0.0375	0.0468	-0.0185
C4				
N3	0.0179	0.0359	0.0269	0.0181
N4	0.0179	0.0359	0.0269	0.0181
O29	0.0625	0.0248	0.0436	-0.0377
O30	0.0625	0.0248	0.0436	-0.0377

**Electron localization function (ELF)**

A reference electron with the same spin as its associated Fermi hole in the same vicinity can be used to determine the probability of locating an electron pair. A description of the spatial localization of these electron pairs can then revealed where a smaller probability

$$\eta = \frac{1}{1 + (\frac{D_{\sigma}}{D_{\sigma,0}})^2} \dots\dots\dots 4$$

$$D_{\sigma,0}(r) = (\frac{3}{5}6\pi^2)^{2/3} [\rho_{\sigma}(r)]^{5/3} \dots\dots\dots 5$$

Equation 5 reveals a description of the kinetic energy density of a homogeneous electron gas with the spin density locally equal to  $\rho_{\sigma}(r)$  where the ELF are restricted to the range  $0 \leq \eta \leq 1$ . If  $\eta = 1$  then the electron is completely localized, and if  $\eta = \frac{1}{2}$ , a homogeneous electron gas-like pair probability (electron delocalization) result. A value close to zero is indicative of the borders between electron pairs (Tsirelson and Stash, 2002). Molecular and atomic shell structures can be clarified through ELF as it provides a topological interpretation of molecular space, which can be helpful to identity regions such as bonds, lone pairs, and core regions (Feixas *et al.*,

induces higher localization of the reference electron. This allows extraction of Information regarding the spatial electron localization from its kinetic energy density through Becke and Edgecombe’s dimensionless scalar electron localization function (ELF) based equation 4 and 5 below.

2015). ELF was investigated for the C-N-O plane (Fig. 24), and it is observed that electrons become more localized at a length > 12.27 Bohr (in the x-direction) in the absence of an aromatic ring for the Ni complexes. The opposite was observed for the Zn complexes. When comparing the Ni to the Zn complexes, electrons become less localized at a length > 14.62 Bohr (in the y-direction) and at a length between 7.51 and 8.70 Bohr (in the y-direction) in C2 from C1. A similar phenomenon was also observed when comparing C3 to C4. In addition to this, electrons also become less localized at a length below 2.43 Bohr (in the y-direction).

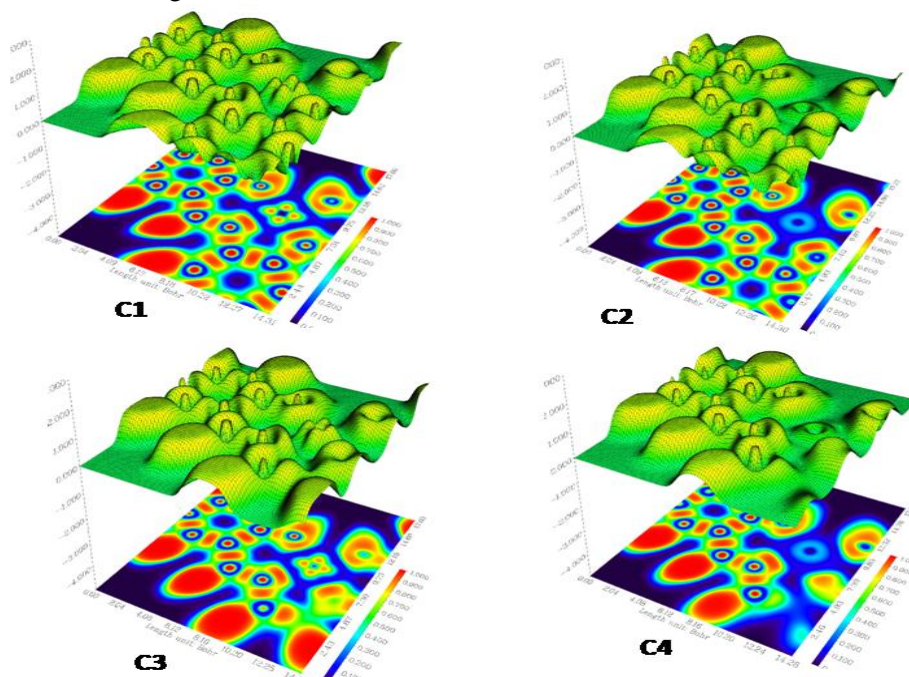


**Figure 24:** Electron localization function maps for the complexes

## CONCLUSION

Four symmetric complexes of Ni(II) and Zn(II) derived from  $N_2O_2$  Schiff bases ligand systems were synthesised using template (*in-situ*) method. The complexes were characterised using various technique relevant for the conformation of molecular structures, with the exception of single crystal X-ray diffraction (SCXRD) analysis. The techniques deployed confirmed the successful synthesis of the complexes, in which one ligand molecules coordinated to the metal ion in a tetra dentate arrangement given rise to perfect square planar and distorted geometries for Ni(II) and Zn(II) complexes respectively. The *in vitro* DPPH radical scavenging and xanthine oxidase inhibitory activity performed

on the complexes comparative to the controls, showed moderate activity on DPPH radical with no or weak activity on xanthine oxidase. In each case, the controls outperformed the complexes on the assays carried out. However, C1 and C4 show some degrees of potency on both the assays at higher concentration. In general, the biological evaluation results (DPPH radical scavenging and xanthine oxidase inhibition) do not provide a solid foundation for a medicinal chemistry approach to fine-tuning the complexes' properties and activity. The DFT calculation of the complexes using M06-2X/B3LYP-311G9d,p level of theory presented electronic properties that supported the experimental findings on the complexes.

## REFERENCES

- Abdel-Rahman, L. H., Adam, M. S. S., Al-Zaqri, N., Shehata, M. R., Ahmed, H. E.-S., & Mohamed, S. K. (2022). Synthesis, characterization, biological and docking studies of ZrO (II), VO (II) and Zn (II) complexes of a halogenated tetra-dentate Schiff base. *Arabian Journal of Chemistry*, *15*(5), 103737.
- Adnan, M. M., Dalod, A. R., Balci, M. H., Glaum, J., & Einarsrud, M.-A. (2018). In situ synthesis of hybrid inorganic-polymer nanocomposites. *Polymers*, *10*(10), 1129.
- Al-Shehri, S. S., Duley, J. A., & Bansal, N. (2020). Xanthine oxidase-lactoperoxidase system and innate immunity: Biochemical actions and physiological roles. *Redox biology*, *34*, 101524.
- Ali, I., Wani, W. A., & Saleem, K. (2013). Empirical formulae to molecular structures of metal complexes by molar conductance. *Synthesis and Reactivity in Inorganic, Metal-Organic, and Nano-Metal Chemistry*, *43*(9), 1162-1170.
- Almagro, P., Boixeda, R., Diez-Manglano, J., Gómez-Antúnez, M., Lopez-Garcia, F., & Recio, J. (2020). Insights into chronic obstructive pulmonary disease as critical risk factor for cardiovascular disease. *International Journal of Chronic Obstructive Pulmonary Disease*, *15*, 755.
- Al-Rabiah, H., Muthu, S., Al-Omary, F., Al-Tamimi, A.-M., Raja, M., Muhamed, R. R., & El-Emam, A. A.-R. (2017). Molecular structure, vibrational spectra, NBO, Fukui function, HOMO-LUMO analysis and molecular docking study of 6-[(2-methylphenyl) sulfanyl]-5-propylpyrimidine-2, 4 (1H, 3H)-dione. *Macedonian Journal of Chemistry and Chemical Engineering*, *36*(1), 59-80.
- Ashiq, K., Naureen, B., & Ashiq, S. (2021). Metal complexes and their potential therapeutic role against COVID-19: recent developments in drug designing. *Sudan Journal of Medical Sciences*, *16*(4), 540-545.

- Battelli, M. G., Polito, L., Bortolotti, M., & Bolognesi, A. (2016). Xanthine oxidoreductase-derived reactive species: physiological and pathological effects. *Oxidative medicine and cellular longevity*, 2016.
- Chattaraj, P. K., & Giri, S. (2009). Electrophilicity index within a conceptual DFT framework. *Annual Reports Section "C"(Physical Chemistry)*, 105, 13-39.
- Chattaraj, P. K., & Roy, D. R. (2007). Update 1 of: electrophilicity index. *Chemical reviews*, 107(9), PR46-PR74.
- Chaudret, R., De Courcy, B., Contreras-Garcia, J., Gloaguen, E., Zehnacker-Rentien, A., Mons, M., & Piquemal, J.-P. (2014). Unraveling non-covalent interactions within flexible biomolecules: from electron density topology to gas phase spectroscopy. *Physical Chemistry Chemical Physics*, 16(21), 9876-9891.
- Chaves, S., Gil, M., Canário, S., Jelic, R., Romao, M. J., Trincao, J., Fresco, P. (2008). Biologically relevant O, S-donor compounds. Synthesis, molybdenum complexation and xanthine oxidase inhibition. *Dalton Transactions* (13), 1773-1782.
- Dehkhodaei, M., Khorshidifard, M., Rudbari, H. A., Sahihi, M., Azimi, G., Habibi, N., Azadbakht, R. (2017). Synthesis, characterization, crystal structure and DNA, HSA-binding studies of four Schiff base complexes derived from salicylaldehyde and isopropylamine. *Inorganica Chimica Acta*, 466, 48-60.
- Demaerel, J., Veryser, C., & De Borggraeve, W. M. (2020). Ex situ gas generation for lab scale organic synthesis. *Reaction Chemistry & Engineering*, 5(4), 615-631.
- Dilmen Portakal, E., Kaya, Y., Demirayak, E., Karacan Yeldir, E., Erçağ, A., & Kaya, İ. (2022). Ni (II), Zn (II), and Fe (III) complexes derived from novel unsymmetrical salen-type ligands: preparation, characterization and some properties. *Journal of Coordination Chemistry*, 1-18.
- Domingo, L. R., & Pérez, P. (2011). The nucleophilicity N index in organic chemistry. *Organic & biomolecular chemistry*, 9(20), 7168-7175.
- Dubois-Deruy, E., Peugnet, V., Turkieh, A., & Pinet, F. (2020). Oxidative stress in cardiovascular diseases. *Antioxidants*, 9(9), 864.
- Elsebach, M., Sierda, E., Goedecke, J. J., Bignardi, L., Hermanowicz, M., Rohde, M., Bazarnik, M. (2020). In Situ Synthesis of Metal-Salophene Complexes on Intercalated Graphene. *The Journal of Physical Chemistry C*, 124(7), 4279-4287.
- Esrabili, M. D., Ghanbari, M., & Mohammadian-Sabet, F. (2014). Substituent effects on cooperativity of pnictogen bonds. *Journal of Molecular Modeling*, 20(9), 1-9.
- Feixas, F., Matito, E., Poater, J., & Solà, M. (2015). Quantifying aromaticity with electron delocalisation measures. *Chemical Society Reviews*, 44(18), 6434-6451.
- Feoli, A. M. P., Macagnan, F. E., Piovesan, C. H., Bodanese, L. C., & Siqueira, I. R. (2014). Xanthine oxidase activity is associated with risk factors for cardiovascular disease and inflammatory and oxidative status markers in metabolic syndrome: effects of a single exercise session. *Oxidative medicine and cellular longevity*, 2014.
- Frisch, M., Trucks, G. W., Schlegel, H. B., Scuseria, G. E., Robb, M. A., Cheeseman, J. R., Petersson, G. (2009). Gaussian 09, revision D. 01: Gaussian, Inc., Wallingford CT.
- Guo, Q., Ghadiri, R., Weigel, T., Aumann, A., Gurevich, E. L., Esen, C., . . . Ostendorf, A. (2014). Comparison of *in situ* and *ex situ* methods for synthesis of two-photon polymerization polymer nanocomposites. *Polymers*, 6(7), 2037-2050.
- Haas, K. L., & Franz, K. J. (2009). Application of metal coordination chemistry to explore and manipulate

- cell biology. *Chemical reviews*, 109(10), 4921-4960.
- Humphrey, W., Dalke, A., & Schulten, K. (1996). VMD: visual molecular dynamics. *Journal of molecular graphics*, 14(1), 33-38.
- Ikram, M., Rehman, S., Khan, A., Baker, R., & Hofer, T. F. Subhan, Schulze, C. (2015). Synthesis, characterization, antioxidant and selective xanthine oxidase inhibitory studies of transition metal complexes of novel amino acid bearing Schiff base ligand. *Inorganica Chimica Acta*, 428, 117-126.
- Jay, R. M., Eckert, S., Fondell, M., Miedema, P. S., Norell, J., Pietzsch, A., . . . Föhlisch, A. (2018). The nature of frontier orbitals under systematic ligand exchange in (pseudo-) octahedral Fe (II) complexes. *Physical Chemistry Chemical Physics*, 20(44), 27745-27751.
- Kargar, H., Adabi Ardakani, A., Munawar, K. S., Ashfaq, M., & Tahir, M. N. (2021). Nickel (II), copper (II) and zinc (II) complexes containing symmetrical Tetradentate Schiff base ligand derived from 3, 5-diiodosalicylaldehyde: Synthesis, characterization, crystal structure and antimicrobial activity. *Journal of the Iranian Chemical Society*, 18(9), 2493-2503.
- Karges, J., Stokes, R. W., & Cohen, S. M. (2021). Metal complexes for therapeutic applications. *Trends in Chemistry*, 3(7), 523-534.
- Kirk, M. L., & Hille, R. (2022). Spectroscopic Studies of Mononuclear Molybdenum Enzyme Centers. *Molecules*, 27(15), 4802.
- Kong, X.-J., He, T., Zhang, Y.-Z., Wu, X.-Q., Wang, S.-N., Xu, M.-M., . . . Li, J.-R. (2019). Constructing new metal-organic frameworks with complicated ligands from "One-Pot" in situ reactions. *Chemical science*, 10(14), 3949-3955.
- Kostova, I., Trendafilova, N., & Momekov, G. (2005). Theoretical and spectroscopic evidence for coordination ability of 3, 3'-benzylidenedi-4-hydroxycoumarin. New neodymium (III) complex and its cytotoxic effect. *Journal of Inorganic biochemistry*, 99(2), 477-487.
- Lewis, D., Ioannides, C., & Parke, D. (1994). Interaction of a series of nitriles with the alcohol-inducible isoform of P450: Computer analysis of structure—activity relationships. *Xenobiotica*, 24(5), 401-408.
- Li, Y.-G., Shi, D.-H., Zhu, H.-L., Yan, H., & Ng, S. W. (2007). Transition metal complexes (M= Cu, Ni and Mn) of Schiff-base ligands: Syntheses, crystal structures, and inhibitory bioactivities against urease and xanthine oxidase. *Inorganica Chimica Acta*, 360(9), 2881-2889.
- Lind, N. M., Joe, N. S., Newell, B. S., & Morris, A. M. (2022). High Yielding, One-Pot Synthesis of Bis (1 H-indazol-1-yl) methane Catalyzed by 3 d-Metal Salts. *Reactions*, 3(1), 59-69.
- Liu, H., Chang, L., Chen, L., & Li, Y. (2015). In situ one-step synthesis of metal-organic framework encapsulated naked Pt nanoparticles without additional reductants. *Journal of Materials Chemistry A*, 3(15), 8028-8033.
- Lu, T., & Chen, F. (2012). Atomic dipole moment corrected Hirshfeld population method. *Journal of Theoretical and Computational Chemistry*, 11(01), 163-183.
- Luo, Q., Lu, C., Liu, L., & Zhu, M. (2022). A review on the synthesis of transition metal nitride nanostructures and their energy related applications. *Green Energy & Environment*.
- Mahmoud, W. A., Hassan, Z. M., & Ali, R. W. (2020). *Synthesis and spectral analysis of some metal complexes with mixed Schiff base ligands 1-[2-(2-hydroxybenzylideneamino) ethyl] pyrrolidine-2, 5-dione (HL1) and (2-hydroxybenzalidine) glycine (HL2)*. Paper presented at the Journal of Physics: Conference Series.
- Milbeo, P., Quintin, F., Moulat, L., Didierjean, C., Martinez, J., Bantreil, X., . . .

- Lamaty, F. (2021). Synthesis, characterisation and cytotoxic activity evaluation of new metal-salen complexes based on the 1, 2-bicyclo [2.2. 2] octane bridge. *Tetrahedron Letters*, 63, 152706.
- Minh, T. N., Van, T. M., Andriana, Y., Vinh, L. T., Hau, D. V., Duyen, D. H., & Guzman-Gelani, C. d. (2019). Antioxidant, xanthine oxidase,  $\alpha$ -amylase and  $\alpha$ -glucosidase inhibitory activities of bioactive compounds from *Rumex crispus* L. root. *Molecules*, 24(21), 3899.
- Nguyen, Q. T., Pham Thi, P. N., & Nguyen, V. T. (2021). Synthesis, characterization, and in vitro cytotoxicity of unsymmetrical tetradentate Schiff base Cu (II) and Fe (III) complexes. *Bioinorganic chemistry and applications*, 2021.
- Nylander, J. A., Wilgenbusch, J. C., Warren, D. L., & Swofford, D. L. (2008). AWTY (are we there yet?): a system for graphical exploration of MCMC convergence in Bayesian phylogenetics. *Bioinformatics*, 24(4), 581-583.
- Oliverio, M., Bulotta, S., & Duarte, N. (2022). Nature Inspired Protective Agents Against Oxidative Stress. *Frontiers in pharmacology*, 13.
- Pahuja, A., Jeyakumar, T. C., & Paularokiadoss, F. (2022). Structural analysis and chemical descriptors analysis of 4-aminopyridine adsorbed on M4 (M= Co, Ni, Cu) clusters: A DFT study. *Vietnam Journal of Chemistry*.
- Parr, R. G., Szentpály, L. v., & Liu, S. (1999). Electrophilicity index. *Journal of the American Chemical Society*, 121(9), 1922-1924.
- Roy, R. K., Krishnamurti, S., Geerlings, P., & Pal, S. (1998). Local softness and hardness based reactivity descriptors for predicting intra-and intermolecular reactivity sequences: carbonyl compounds. *The Journal of Physical Chemistry A*, 102(21), 3746-3755.
- Salih, K. S., Shraim, A. M., Al-Mhini, S. R., Al-Soufi, R. E., & Warad, I. (2021). New tetradentate Schiff base Cu (II) complexes: synthesis, physicochemical, chromotropism, fluorescence, thermal, and selective catalytic oxidation. *Emergent Materials*, 4(2), 423-434.
- Saranya, J., Jone Kirubavathy, S., Chitra, S., Zarrouk, A., Kalpana, K., Lavanya, K., & Ravikiran, B. (2020). Tetradentate Schiff Base complexes of transition metals for antimicrobial activity. *Arabian Journal for Science and Engineering*, 45(6), 4683-4695.
- Sarıkavaklı, N., Söyleyici, H. C., Erol, F., & Omara, T. (2022). Synthesis, characterization and computational studies of 2-amino-4-substituted thiazoles, their divalent nickel and cobalt complexes and molecular docking studies of their ligands as potent  $\mu$ -opioid receptor agonists.
- Sharifi-Rad, M., Anil Kumar, N. V., Zucca, P., Varoni, E. M., Dini, L., Panzarini, E., . . . Peluso, I. (2020). Lifestyle, oxidative stress, and antioxidants: Back and forth in the pathophysiology of chronic diseases. *Frontiers in physiology*, 11, 694.
- Soroceanu, A., & Bargan, A. (2022). Advanced and Biomedical Applications of Schiff-Base Ligands and Their Metal Complexes: A Review. *Crystals*, 12(10), 1436.
- Tamta, H., Kalra, S., & Mukhopadhyay, A. K. (2006). Biochemical characterization of some pyrazolopyrimidine-based inhibitors of xanthine oxidase. *Biochemistry (Moscow)*, 71(1), S49-S54.
- Terraschke, H., Rothe, M., & Lindenberg, P. (2018). In situ monitoring metal-ligand exchange processes by optical spectroscopy and X-ray diffraction analysis: a review. *Reviews in Analytical Chemistry*, 37(1).
- Trzesowska, A., Kruszynski, R., & Bartczak, T. J. (2005). New lanthanide–nitrogen bond-valence parameters. *Acta*

- Crystallographica Section B: Structural Science*, 61(4), 429-434.
- Tsirelson, V., & Stash, A. (2002). Determination of the electron localization function from electron density. *Chemical Physics Letters*, 351(1-2), 142-148.
- Waziri, I., Yusuf, T. L., Akintemi, E., Kelani, M. T., & Muller, A. (2022). Spectroscopic, crystal structure, antimicrobial and antioxidant evaluations of new Schiff base compounds: an experimental and theoretical study. *Journal of Molecular Structure*, 134382.
- Yusuf, T. L., Oladipo, S. D., Zamisa, S., Kumalo, H. M., Lawal, I. A., Lawal, M. M., & Mabuba, N. (2021). Design of new Schiff-Base Copper (II) complexes: Synthesis, crystal structures, DFT study, and binding potency toward cytochrome P450 3A4. *ACS omega*, 6(21), 13704-13718.
- Zhan, C.-G., Nichols, J. A., & Dixon, D. A. (2003). Ionization potential, electron affinity, electronegativity, hardness, and electron excitation energy: molecular properties from density functional theory orbital energies. *The Journal of Physical Chemistry A*, 107(20), 4184-4195.